The Effects of Nonlinear Damping on Post-flutter Behavior Using Geometrically Nonlinear Reduced Order Modeling

by

Pengchao Song

A Thesis Presented in Partial Fulfillment
of the Requirements for the Degree
Master of Science

Approved April 2015 by the
Graduate Supervisory Committee:

Marc Mignolet, Chair
Jay Oswald
Aditi Chattopadhyay

ARIZONA STATE UNIVERSITY

May 2015

ABSTRACT

Recent studies of the occurrence of post-flutter limit cycle oscillations (LCO) of the F-16 have provided good support to the long-standing hypothesis that this phenomenon involves a nonlinear structural damping. A potential mechanism for the appearance of nonlinearity in the damping are the nonlinear geometric effects that arise when the deformations become large enough to exceed the linear regime. In this light, the focus of this investigation is first on extending nonlinear reduced order modeling (ROM) methods to include viscoelasticity which is introduced here through a linear Kelvin-Voigt model in the undeformed configuration. Proceeding with a Galerkin approach, the ROM governing equations of motion are obtained and are found to be of a generalized van der Pol-Duffing form with parameters depending on the structure and the chosen basis functions. An identification approach of the nonlinear damping parameters is next proposed which is applicable to structures modeled within commercial finite element software.

The effects of this nonlinear damping mechanism on the post-flutter response is next analyzed on the Goland wing through time-marching of the aeroelastic equations comprising a rational fraction approximation of the linear aerodynamic forces. It is indeed found that the nonlinearity in the damping can stabilize the unstable aerodynamics and lead to finite amplitude limit cycle oscillations even when the stiffness related nonlinear geometric effects are neglected. The incorporation of these latter effects in the model is found to further decrease the amplitude of LCO even though the dominant bending motions do not seem to stiffen as the level of displacements is increased in static analyses.

ACKNOWLEDGMENTS

I would like to show my sincere gratitude to Dr. Marc Mignolet for all the support and guidance he gave me in this two years. His diligence and optimism motivated me toward the completion of this thesis. The knowledge he shared to me and the influence of his spirit on me are invaluable.

I would also like to thank Dr. Julian Wang for the support on many technological details he patiently gave to me. He has greatly accelerated the completion of this project.

My thanks also goes to Dr. Aditi Chattopadhyay and Dr. Jay Oswald for their serve on my committee.

At last I would like to thank my family and everyone who helped me on the road.

TABLE OF CONTENTS

Page

CHAPTER Page

LIST OF TABLES

Table Page

LIST OF FIGURES

Figure Page

Figure Page

Figure Page

Figure Page

Figure Page

Figure Page

1. INTRODUCTION AND FOCUS

1.1. Post-Flutter Limit Cycle Oscillations and F-16 Investigations

Several current fighter aircraft with external store configurations persistently encounter Limit Cycle Oscillation (LCO) problems. LCO is a self-excited, sustained vibration of limited amplitude which can impact a pilot's control authority over the aircraft, ride quality, and weapon aiming. It can also induce structural fatigue and, under certain circumstances, flutter. Denegri (2000) provided a detailed description of the aircraft/store LCO phenomenon. Norton (1990) gave an excellent overview of LCO for a fighter aircraft carrying external stores and its sensitivity to store carriage configuration and mass properties. Because of this sensitivity, the LCO clearance of a modern fighter aircraft should be addressed for all possible store/weapon configurations. Given the drastic number of such configurations, this effort is a major engineering task in aircraft/store weapon compatibility certification. It requires accurate aeroelastic predictions within a short-time frame as demanded by rapid military responses when facing today’s ever-changing international situation. Further, since there can be thousands of store/weapon combinations for a typical fighter aircraft, the LCO predictions must also be computationally efficient to rapidly identify the critical cases. A robust post-processing procedure is also needed to identify a wide variety of aeroelastic response characteristics including flutter, divergence and LCO.

It is generally believed that LCO of an aircraft with stores is a post flutter phenomenon that belongs to the so-called supercritical LCO mechanism. When the flight condition of the aircraft is beyond its flutter boundary, the aircraft's aeroelastic system is unstable and

a divergent response of the structure occurs if the aeroelastic system is linear. However, if the aeroelastic system is nonlinear and includes a “LCO bounding mechanism” dependent on the amplitude of the structural response, then the growth of the divergent response due to flutter can be limited resulting in LCO at a particular amplitude. The source of the LCO bounding mechanism, which could be from the aerodynamics, structure, or both, still remains to be fully understood and is a long-standing research issue. Many researchers believe that the nonlinearity involved in the LCO bounding mechanism is solely induced by oscillating transonic shocks and/or shock induced flow separation. This type of approach for predicting LCO is defined herein as the sole nonlinear aerodynamic approach. If this is the correct bounding mechanism, the LCO can be predicted using high fidelity Computational Fluid Dynamics (CFD) tools coupled with a linear structural model. Using a CFD tool called the AERO-F/S Suite developed by Farhat (2003), Pasiliao (2012) performed an LCO study on an F-16 with stores configuration that experienced LCO during flight tests and first found good correlation of the onset LCO Mach number (the flutter boundary) between the predicted and flight test measured results. This good matching results from the CFD code accurately capturing the transonic shock effects that normally lower the predicted flutter boundary in transonic flow regions as compared to that predicted by the linear unsteady aerodynamic methods such as the Doublet Lattice Method (DLM) and ZAERO (Chen et al. 1998).

However, even with this good transonic flutter predictive capability, Pasiliao’s investigation failed to predict LCO. On this basis, it appears that the nonlinear aerodynamics provided by the CFD methodology alone is not sufficient as a predictive LCO bounding mechanism. Another sole nonlinear aerodynamic approach was adopted by

Prananta et al. (2003) using the ENFLOW CFD system developed by the National Research Laboratory NLR. It predicted LCO of an F-16 configuration with stores at Mach number (M) = 0.9 and Angle of Attack (AoA) = 7°. However, it is known from the flight observation that the F-16 LCO could occur at cruise angle of attack normally in the range of 2° to 3°. Therefore, it is highly possible that Prananta et al. simulated the oscillating dynamic loads due to wing buffet, but not LCO, on the F-16 at that moderate angle of attack. The strongest evidences to show that the nonlinear aerodynamics cannot be the sole LCO bounding mechanism is the flight test data of two F-16 with store configurations presented by Brignac (1989). Figure 1.1 (a) depicts the flight test LCO data of an F-16 with tip launchers 16S200 at weapon stations 1 and 9 and AIM-7F missiles at weapon stations 3 and 7 presented by Brignac in which the open circles represent no LCO and half solid circles represent the occurrence of LCO observed during flight test. The range of Mach numbers where LCO occurs for this F-16 configuration with stores is within M=0.9 and M=1.4. However, at M=1.4 the transonic shock is absent from the F-16 wing and therefore the LCO bounding mechanism at M=1.4 cannot be induced by the oscillating shock. Another flight test LCO data presented by Brignac and shown in Figure 1.1(b) is a Block 40 F-16 with AIM-9P missiles and LAU-129 launchers at weapon stations 1 and 9, LAU-129 launchers at weapon stations 2 and 8, MK-84 bombs at weapon stations 3 and 7, 370 gallon tanks at weapon stations 4 and 6 and a 300 gallon tank at weapon station 5. The Mach number at which LCO begins for this F-16 configuration with stores is 0.6, which is far below the transonic Mach numbers; showing once again that the LCO bounding mechanism at M=0.6 cannot be the oscillating shock. Therefore, it can be stated that the

sole nonlinear aerodynamic approach supported by a computational methodology cannot adequately address the LCO phenomenon thus far.

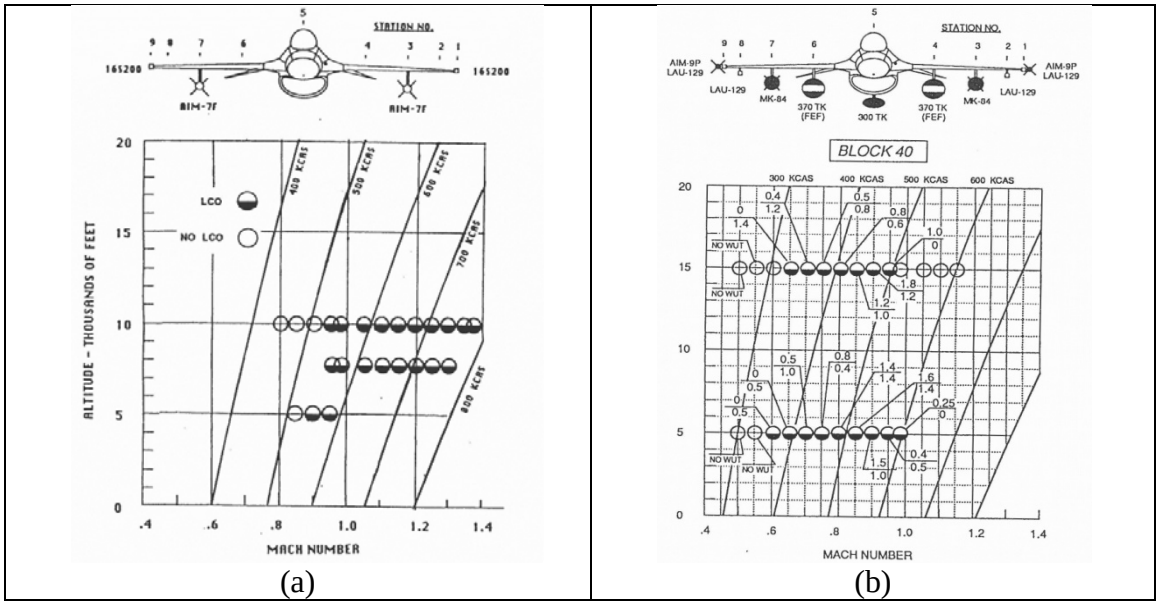

(a) (b)

Figure 1.1. Fight Test LCO Data of an F-16 Configuration with Stores Showing LCO at Mach Numbers from (a) 0.9 to 1.4 and (b) 0.6 to 0.98 (Brignac 1989).

In 1998, nonlinear structural damping was proposed as a LCO bounding mechanism (Chen et al. 1998). The original justification for the appearance of structural nonlinearity was rooted in friction. In this perspective, note first an aircraft with stores consists of many mechanical joints to connect panels to each other, the stores with their respective pylon/launcher and the pylons/launchers to the wing. Further, the dry friction in each mechanical joint could provide a stabilizing nonlinear structural damping to the aeroelastic system. Indeed, when flutter starts and the structural oscillating amplitude is small, the resulting forces due to the low-amplitude oscillation of the joints also are small, smaller than the static friction limit; thus no slip takes place and the oscillating amplitude continues to increase due to flutter. When the amplitude of response becomes large enough, the forces in the mechanical joins are sufficient to induce slip and thus dissipation takes place through

friction. Note that the various joints of the aircraft act in series and thus the occurrence of slip progresses as the amplitude of response increases. Thus, the nonlinear structural damping of the aeroelastic system increases gradually as the oscillating amplitude due to flutter increases. If the flutter mechanism is not explosive, the friction damping in the aeroelastic system (the LCO bounding mechanism) may equate the energy introduced into it through aerodynamics and a LCO may result. This scenario was assessed computationally and experimentally by Choi et al. (2004), Kingsbury et al. (2005) and Choi et al. (2005), and LCO was indeed observed, although as a sub-critical event.

The nonlinear structural damping mechanism is not limited to friction; it can include other forms of damping and dissipation. In fact, Sharma and Denegri (2013) performed a time integration of nonlinear aeroelastic (TINA) equations that includes a prescribed, monotonically increasing nonlinear function of the structural acceleration g at a reference point. During the time-domain simulation, the generalized damping matrix is updated at each time step according to g. The TINA computed LCO amplitudes compared favorably with the flight test data of an F-16 with stores configuration; proving that the nonlinear structural damping mechanism is a strong contender as a LCO bounding mechanism.

1.2. Focus of this Investigation and Thesis Plan

The “larger than usual” amplitudes of response observed in connection with LCO suggest that nonlinear geometric effects may be taking place during these events. This observation provides a physical framework, finite deformation viscoelasticity, for the formal derivation of a nonlinear structural damping model which could generalize and/or replace the postulated functions of (Sharma and Denegri 2013). This effort is the focus of

the present thesis which aims more specifically at developing, and performing a first assessment of, such a nonlinear structural damping model. Given the complexity of dissipation mechanisms in structures, especially assembled ones such as aircraft, it is not expected that this model would be fully predictable using published material constants. Rather, the model is expected to include one or several parameters that would be identified from experiments, as is done in the linear case. The full validation of the proposed model should then be carried out with experimentally measured LCO, e.g. on the F-16, and assess whether it can successfully and consistently predict the observed LCO amplitudes. This validation effort is the subject of a parallel investigation that relies on the approach developed herein. Note that the nonlinear structural damping model development will be accomplished in the framework of nonlinear structural reduced order models (ROMs), see (Mignolet et al. 2013) for a review, and more specifically the approach with dual modes originally proposed in (Kim et al. 2013), see the works of Perez et al. (2014), Kim et al. (2009), Wang et al. (2013) and Perez et al. (2011) for some applications.

The formulation of the proposed nonlinear structural damping model in the context of the nonlinear ROM is described in Chapter 2. Chapter 3 presents the finite element structural and aeroelastic model of the test application, i.e., the heavy Goland wing (Goland and Luke 1948) (Estap et al. 2002). The capability of the proposed nonlinear structural damping to bound the otherwise unstable aeroelastic response is next analyzed in Chapter 4.

2. NONLINEAR STRUCTURAL REDUCED ORDER MODELING

2.1. Chapter Overview

The focus of this chapter is primarily on the derivation of a nonlinear structural damping model which is consistent with the larger than linear deformations that are expected during LCO events. In section 2.2, this model is developed from finite deformation viscoelasticty in a reduced order format consistent with mode-based aeroelasticity analyses (e.g., see discussion of section 3.2). The identification of the parameters of this model from a finite element representation of the structure performed in a commercial software, e.g., Nastran, Abaqus, is next considered. Identifying the stiffness parameters has been achieved in prior publications, e.g., see the works of Muravyov et al (2003), Mignolet et al (2013), Kim et al (2013) and section 2.3, but the corresponding effort for the damping parameters is novel. To this end, a parallel between the parameters of the nonlinear damping model and the nonlinear stiffness coefficients associated with the geometric nonlinearity is first demonstrated, see section 2.4, and the identification of the nonlinear damping model based on this parallel is formulated.

2.2. Nonlinear Geometric Viscoelastic Modeling

As stated in the introduction, the framework for the derivation of the nonlinear structural damping model is finite deformation viscoelasticity. To proceed, let the position vector of a point of the structure denoted by $\underline{X}$ in the reference configuration and as $\underline{x}$ in the deformed one so that the displacement vector is $\underline{u} = \underline{x} - \underline{X}$, see Figure 2.1. Define next the deformation gradient tensor $\underline{\underline{F}}$ of components F_{ij} as

$$F_{ij} = \frac{\partial x_i}{\partial X_j} = \delta_{ij} + \frac{\partial u_i}{\partial X_j} \tag{2.1}$$

where δ_{ij} denotes the Kronecker symbol. The deformations of the structure will be quantified by the Green strain tensor $\underline{\underline{E}}$ the components of which are

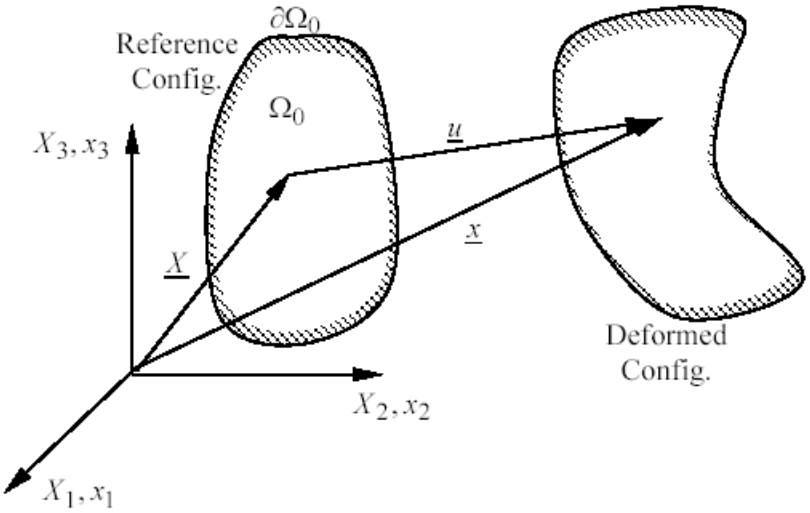

Figure 2.1. Reference and Deformed Configurations (Fung and Tong 2001)

$$E_{ij} = \frac{1}{2}\left(F_{ki}\, F_{kj} - \delta_{ij}\right). \tag{2.2}$$

Note in the above equation and in the remainder of this thesis that summation is implied on all repeated indices.

In the reference configuration, the equation of motion of the structure are (Fung and Tong 2001) (Bonet and Wood 1997):

$$\frac{\partial}{\partial X_k}\left(F_{ij}\, S_{jk}\right) + \rho_0\, b_i^0 = \rho_0\, \ddot{u}_i \quad \text{for} \quad \underline{X} \in \Omega_0 \tag{2.3}$$

where $\underline{\underline{S}}$ denotes the second Piola-Kirchhoff stress tensor, $\rho_0(\underline{X})$ is the density in the reference configuration, and $\underline{b}^0$ is the vector of body forces, all of which may depend on

the coordinates X_i. Finally, Ω_0 is the domain occupied by the structure in the reference configuration and $\partial\Omega_0$ is its boundary.

To complete Eq. (2.3), it remains to specify the constitutive behavior of the material, i.e., relate the second Piola-Kirchhoff $\underline{\underline{S}}$ to the Green strain tensor $\underline{\underline{E}}$. Since a damping/dissipation model is the goal of the present derivation, an elastic behavior is not sufficient, rather a viscoelastic constitutive model is necessary. Specifically, a Kelvin-Voigt model will be assumed so that

$$S_{ij} = C_{ijkl}\, E_{kl} + D_{ijkl}\, \dot{E}_{kl} \tag{2.4}$$

where $\underline{\underline{C}}$ and $\underline{\underline{D}}$ the fourth order elasticity and dissipation tensors $\underline{\underline{C}}$ where the former satisfies the symmetry conditions

$$C_{ijkl} = C_{jikl} = C_{ijlk} \qquad C_{ijkl} = C_{klij} \tag{2.5}$$

and the positive definiteness property

$$A_{ij}\, C_{ijkl}\, A_{kl} > 0 \tag{2.6}$$

for any non zero second order tensor $\underline{\underline{A}}$. To ensure that dissipation takes place at all times for all possible deformation velocities, it is required that

$$\dot{E}_{ij}\, D_{ijkl}\, \dot{E}_{kl} > 0 \tag{2.7}$$

that is, $\underline{\underline{D}}$ must be positive definite.

A reduced order model of the above problem can be developed by expressing the displacement field $u_i(\underline{X}, t)$ as an expansion over basis functions $U_i^{(n)}(\underline{X})$ that do not change with time and automatically satisfy the geometric boundary conditions (assumed here to be homogenous). That is,

$$u_i(\underline{X},t) = q_n(t)\, U_i^{(n)}(\underline{X}) \tag{2.8}$$

where $q_n(t)$ are the time dependent generalized coordinates. Introducing this representation in Eq. (2.1) leads to

$$F_{ij} = \delta_{ij} + q_n \frac{\partial U_i^{(n)}}{\partial X_j} \tag{2.9}$$

where the dependences of q_n on time and $U_i^{(n)}$ on the position $\underline{X}$ have been suppressed for notational simplicity. Combining Eqs (2.9) and (2.2) leads to the following expression for the components of the Green strain tensor

$$E_{ij} = q_n \frac{1}{2}\left[\frac{\partial U_i^{(n)}}{\partial X_j} + \frac{\partial U_j^{(n)}}{\partial X_i}\right] + q_n\, q_m \frac{1}{2} \frac{\partial U_k^{(n)}}{\partial X_i} \frac{\partial U_k^{(m)}}{\partial X_j}. \tag{2.10}$$

Differentiating this expression with respect to time and recombining terms leads to

$$\dot{E}_{ij} = \dot{q}_n \frac{1}{2}\left[\frac{\partial U_i^{(n)}}{\partial X_j} + \frac{\partial U_j^{(n)}}{\partial X_i}\right] + \dot{q}_n\, q_m \frac{1}{2}\left[\frac{\partial U_k^{(n)}}{\partial X_i} \frac{\partial U_k^{(m)}}{\partial X_j} + \frac{\partial U_k^{(m)}}{\partial X_i} \frac{\partial U_k^{(n)}}{\partial X_j}\right]. \tag{2.11}$$

The derivation of the corresponding ROM governing equations stems from imposing Eq. (2.3). Note however that this equation cannot be satisfied at every point $\underline{X}$ as the representation of Eq. (2.8) is finite dimensional (finite number of generalized coordinates). To resolve this issue, a Galerkin approach is adopted in which the residual of Eq. (2.3) after imposing Eq. (2.8) is required to be orthogonal to the basis functions $U_i^{(n)}(\underline{X})$. That is,

$$\int_{\Omega_0} \left[\rho_0\, \ddot{u}_i - \frac{\partial}{\partial X_k}\left(F_{ij}\, S_{jk}\right) - \rho_0\, b_i^0\right] U_i^{(n)}\, d\underline{X} = 0\,. \tag{2.12}$$

Next, using the divergence theorem, one finds

$$\int_{\Omega_0} \frac{\partial}{\partial X_k}\left(F_{ij}\, S_{jk}\right) U_i^{(n)}\, d\underline{X} = -\int_{\Omega_0} F_{ij}\, S_{jk}\, \frac{\partial U_i^{(n)}}{\partial X_k}\, d\underline{X} + \int_{\partial\Omega_0} F_{ij}\, S_{jk}\, U_i^{(n)} dX_k \ . \quad (2.13)$$

Combining Eqs (2.12), (2.13), and (2.8) leads to the ROM governing equations

$$M_{mn}\, \ddot{q}_n + f_m(q, \dot{q}) = F_m \quad (2.14)$$

where

$$M_{mn} = \int_{\Omega_0} \rho_0\, U_i^{(m)}\, U_i^{(n)} d\underline{X} \quad (2.15)$$

are the components of the mass matrix, F_m are the modal forces resulting from both body forces and surface tractions as

$$F_m = \int_{\Omega_0} \rho_0\, b_i^0\, U_i^{(n)}\, d\underline{X} + \int_{\partial\Omega_0} F_{ij}\, S_{jk}\, U_i^{(n)} dX_k \quad (2.16)$$

and finally

$$f_m(q, \dot{q}) = \int_{\Omega_0} F_{ij}\, S_{jk}\, \frac{\partial U_i^{(m)}}{\partial X_k}\, d\underline{X} = \int_{\Omega_0} C_{jkrs}\, F_{ij}\, E_{rs}\, \frac{\partial U_i^{(m)}}{\partial X_k}\, d\underline{X} + \int_{\Omega_0} D_{jkrs}\, F_{ij}\, \dot{E}_{rs}\, \frac{\partial U_i^{(m)}}{\partial X_k}\, d\underline{X} \ . \quad (2.17)$$

The above nonlinear term can be expressed explicitly in terms of the generalized coordinates q_n and their derivatives $\dot{q}_n$ by using Eqs (2.9)-(2.11). Specifically, it is found that

$$f_m(q, \dot{q}) = K_{mn}^{(1)}\, q_n + K_{mnl}^{(2)}\, q_n\, q_l + K_{mnlp}^{(3)}\, q_n\, q_l\, q_p + D_{mn}^{(1)}\, \dot{q}_n + D_{mjn}^{(2)}\, q_j\, \dot{q}_n + D_{mlpn}^{(3)}\, q_l\, q_p\, \dot{q}_n \quad (2.18)$$

where

$$K_{mn}^{(1)} = \int_{\Omega_0} C_{jkrs}\,\delta_{ij}\,\frac{1}{2}\left[\frac{\partial U_r^{(n)}}{\partial X_s} + \frac{\partial U_s^{(n)}}{\partial X_r}\right]\frac{\partial U_i^{(m)}}{\partial X_k}\,d\underline{X} = \int_{\Omega_0} C_{ikrs}\,\frac{\partial U_r^{(n)}}{\partial X_s}\,\frac{\partial U_i^{(m)}}{\partial X_k}\,d\underline{X} \tag{2.19}$$

$$\begin{aligned} K_{mnl}^{(2)} &= \int_{\Omega_0} C_{jkrs}\delta_{ij}\,\frac{1}{2}\,\frac{\partial U_p^{(n)}}{\partial X_r}\,\frac{\partial U_p^{(l)}}{\partial X_s}\,\frac{\partial U_i^{(m)}}{\partial X_k}\,d\underline{X} + \int_{\Omega_0} C_{jkrs}\frac{\partial U_i^{(l)}}{\partial X_j}\,\frac{1}{2}\left[\frac{\partial U_r^{(n)}}{\partial X_s} + \frac{\partial U_s^{(n)}}{\partial X_r}\right]\frac{\partial U_i^{(m)}}{\partial X_k}\,d\underline{X} \\ &= \frac{1}{2}\hat{K}_{mnl}^{(2)} + \hat{K}_{nlm}^{(2)} \end{aligned} \tag{2.20}$$

where

$$\hat{K}_{mnp}^{(2)} = \hat{K}_{mpn}^{(2)} = \int_{\Omega_0} \frac{\partial U_i^{(m)}}{\partial X_j}\,C_{ijkl}\,\frac{\partial U_r^{(n)}}{\partial X_k}\,\frac{\partial U_r^{(p)}}{\partial X_l}\,d\underline{X} \tag{2.21}$$

$$K_{mnlp}^{(3)} = \int_{\Omega_0} C_{jkrs}\frac{\partial U_i^{(n)}}{\partial X_j}\,\frac{1}{2}\,\frac{\partial U_v^{(l)}}{\partial X_r}\,\frac{\partial U_v^{(p)}}{\partial X_s}\,\frac{\partial U_i^{(m)}}{\partial X_k}\,d\underline{X} = \frac{1}{2}\int_{\Omega_0} \frac{\partial U_i^{(m)}}{\partial X_j}\,\frac{\partial U_i^{(n)}}{\partial X_k}\,C_{jkrs}\frac{\partial U_v^{(l)}}{\partial X_r}\,\frac{\partial U_v^{(p)}}{\partial X_s}\,d\underline{X} \tag{2.22}$$

in which the symmetry properties of Eq. (2.5) have been used to regroup similar terms. Assuming that similar symmetry properties hold for the dissipation tensor, i.e.,

$$D_{ijkl} = D_{jikl} = D_{ijlk} \qquad D_{ijkl} = D_{klij} \tag{2.23}$$

one obtains

$$D_{mn}^{(1)} = \int_{\Omega_0} D_{jkrs}\,\delta_{ij}\,\frac{1}{2}\left[\frac{\partial U_r^{(n)}}{\partial X_s} + \frac{\partial U_s^{(n)}}{\partial X_r}\right]\frac{\partial U_i^{(m)}}{\partial X_k}\,d\underline{X} = \int_{\Omega_0} D_{ikrs}\,\frac{\partial U_r^{(n)}}{\partial X_s}\,\frac{\partial U_i^{(m)}}{\partial X_k}\,d\underline{X} \tag{2.24}$$

$$D^{(2)}_{mln} = \int_{\Omega_0} D_{jkrs}\,\delta_{ij}\,\frac{1}{2}\left[\frac{\partial U^{(n)}_p}{\partial X_r}\frac{\partial U^{(l)}_p}{\partial X_s}+\frac{\partial U^{(l)}_p}{\partial X_r}\frac{\partial U^{(n)}_p}{\partial X_s}\right]\frac{\partial U^{(m)}_i}{\partial X_k}\,d\underline{X}$$
$$+\int_{\Omega_0} D_{jkrs}\,\frac{\partial U^{(l)}_i}{\partial X_j}\,\frac{1}{2}\left[\frac{\partial U^{(n)}_r}{\partial X_s}+\frac{\partial U^{(n)}_s}{\partial X_r}\right]\frac{\partial U^{(m)}_i}{\partial X_k}\,d\underline{X} = \hat{D}^{(2)}_{mnl}+\hat{D}^{(2)}_{nlm} \tag{2.25}$$

where

$$\hat{D}^{(2)}_{mnp} = \hat{D}^{(2)}_{mpn} = \int_{\Omega_0} \frac{\partial U^{(m)}_i}{\partial X_j} D_{ijkl}\,\frac{\partial U^{(n)}_r}{\partial X_k}\frac{\partial U^{(p)}_r}{\partial X_l}\,d\underline{X} \tag{2.26}$$

and

$$D^{(3)}_{mpln} = \int_{\Omega_0} D_{jkrs}\,\frac{\partial U^{(p)}_i}{\partial X_j}\,\frac{1}{2}\left[\frac{\partial U^{(n)}_v}{\partial X_r}\frac{\partial U^{(l)}_v}{\partial X_s}+\frac{\partial U^{(n)}_v}{\partial X_s}\frac{\partial U^{(l)}_v}{\partial X_r}\right]\frac{\partial U^{(m)}_i}{\partial X_k}\,d\underline{X}$$
$$= \int_{\Omega_0} \frac{\partial U^{(m)}_i}{\partial X_j}\,\frac{\partial U^{(p)}_i}{\partial X_k} D_{jkrs}\,\frac{\partial U^{(l)}_v}{\partial X_r}\frac{\partial U^{(n)}_v}{\partial X_s}\,d\underline{X} \tag{2.27}$$

.

In carrying out the final assembly of the ROM equations, it should be recognized that the contributions of the terms $K^{(2)}_{mnl}\,q_n\,q_l$ and $K^{(2)}_{m\ln}\,q_l\,q_n$ can be combined to each other and similarly for other cubic terms. This process leads to the equivalent expression

$$f_m(q,\dot{q}) = K^{(1)}_{mn}\,q_n + \overline{K}^{(2)}_{mnl}\,q_n\,q_l + \overline{K}^{(3)}_{mnlp}\,q_n\,q_l\,q_p + D^{(1)}_{mn}\,\dot{q}_n + D^{(2)}_{mjn}\,q_j\,\dot{q}_n + \overline{D}^{(3)}_{mlpn}\,q_l\,q_p\,\dot{q}_n \tag{2.28}$$

where

$$\overline{K}^{(2)}_{mnl} = \begin{cases} 0 & \text{for } l < n \\ K^{(2)}_{mnn} = \dfrac{1}{2}\hat{K}^{(2)}_{mnn} + \hat{K}^{(2)}_{nnm} & \text{for } l = n \\ K^{(2)}_{mnl} + K^{(2)}_{mln} = \hat{K}^{(2)}_{mnl} + \hat{K}^{(2)}_{nlm} + \hat{K}^{(2)}_{lnm} & \text{for } l > n \end{cases} \tag{2.29}$$

$$\overline{K}^{(3)}_{mnlp} = \begin{cases} 0 & \text{unless } p \geq l \geq n \\ K^{(3)}_{mnnn} & \text{for } p = l = n \\ K^{(3)}_{mnll} + K^{(3)}_{mlnl} + K^{(3)}_{mlln} & \text{for } p = l > n \\ K^{(3)}_{mpll} + K^{(3)}_{mlpl} + K^{(3)}_{mllp} & \text{for } p > l = n \\ 2K^{(3)}_{mnlp} + 2K^{(3)}_{mpln} + 2K^{(3)}_{mlpn} & \text{for } p > l > n \end{cases} \tag{2.30}$$

recognizing the properties

$$K^{(3)}_{mnlp} = K^{(3)}_{nmlp} = K^{(3)}_{mnpl} = K^{(3)}_{lpmn} \tag{2.31}$$

resulting from Eqs (2.5) and (2.22), and

$$\overline{D}^{(3)}_{mlpn} = \begin{cases} 0 & \text{for } p < l \\ D^{(3)}_{mlln} & \text{for } p = l \\ D^{(3)}_{mlpn} + D^{(3)}_{mpln} & \text{for } p > l \end{cases} . \tag{2.32}$$

The final resulting ROM governing equations are thus

$$M_{mn}\,\ddot{q}_n + K^{(1)}_{mn}\,q_n + \overline{K}^{(2)}_{mnl}\,q_n\,q_l + \overline{K}^{(3)}_{mnlp}\,q_n\,q_l\,q_p + D^{(1)}_{mn}\,\dot{q}_n + D^{(2)}_{m\ln}\,q_l\,\dot{q}_n + \overline{D}^{(3)}_{mlpn} q_l\,q_p\,\dot{q}_n = F_m \tag{2.33}$$

Some properties of the tensors M_{mn}, $K^{(1)}_{mn}$, $K^{(2)}_{mnl}$, $K^{(3)}_{mnlp}$, $D^{(1)}_{mn}$, $D^{(2)}_{mln}$, and $D^{(3)}_{mlpn}$ that reflect those of the elasticity and dissipation tensors have already been stated above, e.g, Eq. (2.31). In addition, the following symmetry properties can also be recognized

$$M_{mn} = M_{nm} \quad K^{(1)}_{mn} = K^{(1)}_{nm} \qquad D^{(1)}_{mn} = D^{(1)}_{nm} \tag{2.34}$$

and

$$D^{(3)}_{mnlp} = D^{(3)}_{nmlp} = D^{(3)}_{mnpl} = D^{(3)}_{lpmn}. \tag{2.35}$$

With regard to positive definiteness, a property involving the tensors $K^{(1)}_{mn}$, $K^{(2)}_{mnl}$, and $K^{(3)}_{mnlp}$ has been proved in (Mignolet et al 2008). For a similar condition relating to the damping terms, introduce the tangent damping matrix $D^{(T)}(q)$ of elements

$$D^{(T)}_{mn} = D^{(1)}_{mn} + D^{(2)}_{mln}\, q_l + D^{(3)}_{mlpn}\, q_l\, q_p\,. \tag{2.36}$$

Since the tensor $\underline{\underline{D}}$ is positive definite, dissipation takes place continuously and thus one expects that $D^{(T)}(q)$ is a positive definite matrix. Indeed, note that

$$\begin{aligned}
&\dot{q}_m\, D^{(T)}_{mn}\, \dot{q}_n = \dot{q}_m\, D^{(1)}_{mn}\, \dot{q}_n + \dot{q}_m\, D^{(2)}_{mln}\, q_l\, \dot{q}_n + \dot{q}_m\, D^{(3)}_{mlpn}\, q_l\, q_p\, \dot{q}_n \\
&= \int_{\Omega_0} \left[\dot{q}_m \frac{\partial U^{(m)}_i}{\partial X_k} \right] D_{ikrs} \left[\dot{q}_n \frac{\partial U^{(n)}_r}{\partial X_s} \right] d\underline{X} + \int_{\Omega_0} \left[\dot{q}_m \frac{\partial U^{(m)}_i}{\partial X_j} \right] D_{ijks} \left[q_l\, \dot{q}_n \frac{\partial U^{(n)}_r}{\partial X_k} \frac{\partial U^{(l)}_r}{\partial X_s} \right] d\underline{X} \\
&\quad + \int_{\Omega_0} \left[\dot{q}_n \frac{\partial U^{(n)}_i}{\partial X_j} \right] D_{ijks} \left[q_l\, \dot{q}_m \frac{\partial U^{(l)}_r}{\partial X_k} \frac{\partial U^{(m)}_r}{\partial X_s} \right] d\underline{X} \\
&\quad + \int_{\Omega_0} \left[q_p\, \dot{q}_m \frac{\partial U^{(m)}_i}{\partial X_j} \frac{\partial U^{(p)}_i}{\partial X_k} \right] D_{jkrs} \left[q_l\, \dot{q}_n \frac{\partial U^{(l)}_v}{\partial X_r} \frac{\partial U^{(n)}_v}{\partial X_s} \right] d\underline{X} \\
&= \int_{\Omega_0} W_{ik}\, D_{ikrs}\, W_{rs}\, d\underline{X} = \int_{\Omega_0} \dot{E}_{ik}\, D_{ikrs}\, \dot{E}_{rs}\, d\underline{X} \geq 0
\end{aligned} \tag{2.37}$$

where

$$W_{ik} = \dot{q}_m \frac{\partial U^{(m)}_i}{\partial X_k} + q_p\, \dot{q}_m \frac{\partial U^{(m)}_j}{\partial X_i} \frac{\partial U^{(p)}_j}{\partial X_k}\,. \tag{2.38}$$

2.3. Non-Intrusive Identification of the Stiffness Parameters

Equations (2.19)-(2.22) provide direct expressions for all stiffness parameters of the reduced order model parameters in terms of the basis functions $U_i^{(m)}(\underline{X})$ and the geometrical and material properties of the structure, e.g. ρ_0, C_{ijkl}, Ω_0, etc. While these equations can indeed be used efficiently (Capiez-Lernout et al 2014) (Capiez-Lernout et al 2012), they require the details of the finite element mesh and formulation. When using a commercial finite element software, it is much more convenient to proceed in an indirect or non-intrusive manner by relating the parameters to be determined to a nonlinear static finite element solution, for example as proposed in (Muravyov and Rizzi 2003) with the modification of (Kim et al 2013).

This approach (i) proceeds with the imposition of specific displacement fields, (ii) obtains from the finite element software the set of nodal forces required to achieve these displacements, (iii) projects these forces on the basis functions, and (iv) imposes that the displacements and modal forces satisfy Eq. (2.33). The first set of imposed displacements are proportional to one particular basis function, the *n*th one, $U_i^{(n)}(\underline{X})$, say. Three such displacement fields

$$\bar{u}_i^{(1)}(\underline{X}) = q_n^{(1)}\ U_i^{(n)}(\underline{X});\ \ \bar{u}_i^{(2)}(\underline{X}) = q_n^{(2)}\ U_i^{(n)}(\underline{X}) \ \text{ and } \ \bar{u}_i^{(3)}(\underline{X}) = q_n^{(3)}\ U_i^{(n)}(\underline{X}) \tag{2.39}$$

are imposed where $q_n^{(1)}, q_n^{(2)}$, and $q_n^{(3)}$ are constants scaling factors differing from each other. These factors are selected so that the displacements induced are large enough to induce significant geometric nonlinear effects but small enough to stay within the

convergence limits of the finite element code. Imposing these displacements requires a set of nodal forces which can be outputted by many commercial finite element codes (e.g., Nastran, Abaqus, DYNA-3D). Projecting these nodal forces on the *m*th basis function leads to modal forces $F_m^{n(p)}$, *p*=1, 2, or 3. Consistently with Eq. (2.33), the imposed displacement fields and modal forces must satisfy the equations

$$K_{mn}^{(1)}\ q_n^{(1)} + \overline{K}_{mnn}^{(2)}\left(q_n^{(1)}\right)^2 + \overline{K}_{mnnn}^{(3)}\left(q_n^{(1)}\right)^3 = F_m^{n(1)} \tag{2.40}$$

$$K_{mn}^{(1)}\ q_n^{(2)} + \overline{K}_{mnn}^{(2)}\left(q_n^{(2)}\right)^2 + \overline{K}_{mnn}^{(3)}\left(q_n^{(2)}\right)^3 = F_m^{n(2)} \tag{2.41}$$

$$K_{mn}^{(1)}\ q_n^{(3)} + \overline{K}_{mnn}^{(2)}\left(q_n^{(3)}\right)^2 + \overline{K}_{mnnn}^{(3)}\left(q_n^{(3)}\right)^3 = F_m^{n(3)} \tag{2.42}$$

The above equations represent, for each *m* and *n*, a set of three linear equations in the unknown $K_{mn}^{(1)}, \overline{K}_{mnn}^{(2)}$, and $\overline{K}_{mnnn}^{(3)}$ which is readily solved.

The next stage in the identification algorithm focuses on the determination of the parameters $K_{mnp}^{(2)}$, $\overline{K}_{mnnp}^{(3)}$, and $\overline{K}_{mnpp}^{(3)}$ with $p > n$. This effort is achieved by imposing displacement fields which are linear combinations of the basis functions *n* and *p*, i.e.

$$\overline{u}_i^{(4)}\left(\underline{X}\right) = q_n^{(4)}\ U_i^{(n)}\left(\underline{X}\right) + q_p^{(4)}\ U_i^{(p)}\left(\underline{X}\right);$$

$$\overline{u}_i^{(5)}\left(\underline{X}\right) = q_n^{(5)}\ U_i^{(n)}\left(\underline{X}\right) + q_p^{(5)}\ U_i^{(p)}\left(\underline{X}\right)$$

and $$\overline{u}_i^{(6)}\left(\underline{X}\right) = q_n^{(6)}\ U_i^{(n)}\left(\underline{X}\right) + q_p^{(6)}\ U_i^{(p)}\left(\underline{X}\right). \tag{2.43}$$

Imposing the validity of the ROM governing equation, Eq. (2.33), for these 3 displacement fields and their associated modal force $F_i^{n(p)}$, *p* = 4, 5, and 6, yields a set of three equations for each *m*, *n*, and *p* which is readily solved to obtain the parameters $\overline{K}_{mnp}^{(2)}$,

$\overline{K}^{(3)}_{mnnp}$, and $\overline{K}^{(3)}_{mnpp}$. The selection $q^{(4)}_n = q^{(5)}_n = -q^{(6)}_n$ and $q^{(4)}_m = -q^{(5)}_m = -q^{(6)}_m$ is usually achieved as it leads to some simplifications of the equations.

The final step of the algorithm is the identification of the parameters $\overline{K}^{(3)}_{mnps}$ for $s > p > n$. It is carried out from the set of modal forces $F^{(7)}_m$ corresponding to the displacement field

$$\bar{u}^{(7)}_i(\underline{X}) = q^{(7)}_n \, U^{(n)}_i(\underline{X}) + q^{(7)}_p \, U^{(p)}_i(\underline{X}) + q^{(7)}_s \, U^{(s)}_i(\underline{X}) \tag{2.44}$$

and the previously identified stiffnesses.

It should be noted that the above identification procedure does not identify the parameters $K^{(2)}_{mnp}$ or $K^{(3)}_{mnps}$ but rather $\overline{K}^{(2)}_{mnp}$ and $\overline{K}^{(3)}_{mnps}$. From the standpoint of computing the response of the structure using the reduced order model, this is however fully appropriate as the latter parameters are the ones that appear in Eq. (2.33).

2.4. Non-Intrusive Identification of the Damping Parameters – A Parallel

The final step of the nonlinear reduced order modeling effort is the evaluation of the linear and nonlinear damping parameters $D^{(1)}_{mn}$, $D^{(2)}_{mln}$, and $\overline{D}^{(3)}_{mlpn}$. In that regard, a strategy similar to the one carried out in section 2.3 for the identification of the stiffness parameters could be construed. It would involve imposing *velocity* fields and determining the possibly *time-dependent* forces necessary on a structure exhibiting a Kelvin-Voigt viscoelastic constitutive relation. This approach was not pursued here as it would require more expensive transient solutions and would require an appropriate handling (i.e,, setting

up the computations so that they vanish or evaluating them accurately) of the inertia and stiffness terms.

Rather, an alternative approach was followed that relies on the similarities between damping and stiffness parameters. Indeed, comparing Eqs (2.19) and (2.24), it is seen that $D^{(1)}_{mn}$ and $K^{(1)}_{mn}$ are identically computed from the dissipation and elasticity tensors D_{ijkl} and C_{ijkl}, respectively. Thus, if one was to carry out the identification effort of section 2.3 with the numerical values of a fictitious elasticity tensor matching those of the dissipation tensor (note that their units are different), one would find that the identified linear stiffness matrix matches the linear damping one. Since the properties assumed here of the dissipation tensor match those of the elasticity tensor, this computation is meaningful.

The overall plan for the identification of the damping parameters is thus as follows:

<u>STEP 1:</u> Perform the identification of the stiffness parameters ${}_D K^{(1)}_{mn}$, ${}_D \overline{K}^{(2)}_{mnp}$, and ${}_D \overline{K}^{(3)}_{mnps}$ using the elasticity tensor C_{ijkl} numerically equal to D_{ijkl}. The parameters ${}_D K^{(1)}_{mn}$, ${}_D \overline{K}^{(2)}_{mnp}$, and ${}_D \overline{K}^{(3)}_{mnps}$ will be referred to as the pseudo stiffness parameters as their units are not consistent with stiffnesses.

<u>STEP 2:</u> Determine the damping parameters $D^{(1)}_{mn}$, $D^{(2)}_{mln}$, and $\overline{D}^{(3)}_{mlpn}$ from the pseudo stiffness parameters ${}_D K^{(1)}_{mn}$, ${}_D \overline{K}^{(2)}_{mnp}$, and ${}_D \overline{K}^{(3)}_{mnps}$.

While the above approach is straightforward for the linear terms and yields, as suggested above,

$$D^{(1)}_{mn} = {}_D K^{(1)}_{mn}, \tag{2.45}$$

additional discussion is necessary for the quadratic and cubic parameters $D^{(2)}_{mln}$ and $\overline{D}^{(3)}_{mlpn}$. Indeed, the connectivity between stiffness and damping parameters is not between $D^{(2)}_{mln}$ and ${}_D\overline{K}^{(2)}_{mnp}$ but rather between $\hat{D}^{(2)}_{mln}$ and ${}_D\hat{K}^{(2)}_{mnp}$. Specifically, comparing Eqs (2.21) and (2.6) one obtains

$$\hat{D}^{(2)}_{mnp} = {}_D\hat{K}^{(2)}_{mnp}. \tag{2.46}$$

Similarly, one find from Eq. (2.22) and (2.27) that

$$D^{(3)}_{mpln} = 2\ {}_DK^{(3)}_{mpln}. \tag{2.47}$$

Thus, to use the above correspondences, it is necessary to first determine ${}_D\hat{K}^{(2)}_{mnp}$ from ${}_D\overline{K}^{(2)}_{mnp}$ and similarly ${}_D\overline{K}^{(3)}_{mnps}$ from ${}_DK^{(3)}_{mnps}$ by "inverting" Eqs (2.29) and (2.30) (note that a direct estimation approach of ${}_D\hat{K}^{(2)}_{mnp}$ and ${}_DK^{(3)}_{mnps}$ is currently being assessed in a parallel investigation (Wang and Mignolet 2015). However, this inversion is, in general, *not possible* – at least not without further assumptions.

The wing considered in this investigation (see Chapter 3 for details) is flat and symmetric through thickness. For such models, it has been shown (Mignolet et al 2013) (Mignolet and Soize 2008) that (i) the basis is composed of purely transverse (subscript "*t*") and purely in-plane (subscript "*d*" for the dual modes, see (Mignolet et al 2013), (Kim et al 2013) and Chapter 4) functions and (ii) all parameters $\hat{K}^{(2)}_{mnp}$ are zero *except* when *m* denotes a dual mode (in-plane) and the basis functions *n* and *p* are both transverse (equal or different) modes. Then, from Eq. (2.29), one has

$$ {}_D\hat{K}^{(2)}_{dt_2t_1} = {}_D\overline{K}^{(2)}_{dt_1t_2} \qquad \text{and} \qquad {}_D\hat{K}^{(2)}_{dt_1t_2} = {}_D\overline{K}^{(2)}_{dt_1t_2} \qquad \text{for} \quad t_2 > t_1 \tag{2.48} $$

and

$$ {}_D\hat{K}^{(2)}_{dt_1t_2} = 2\ {}_D\overline{K}^{(2)}_{dt_1t_2} \qquad \text{for} \quad t_2 = t_1 \tag{2.49} $$

Finally, propagating this result through Eqs (2.46) and (2.25) leads to

$$ D^{(2)}_{dt_1t_2} = {}_D\overline{K}^{(2)}_{dt_1t_2} \qquad \text{and} \qquad D^{(2)}_{dt_2t_1} = {}_D\overline{K}^{(2)}_{dt_1t_2} \qquad \text{for} \quad t_2 > t_1 \tag{2.50} $$

and

$$ D^{(2)}_{dt_1t_2} = 2\ {}_D\overline{K}^{(2)}_{dt_1t_2} \qquad \text{for} \quad t_2 = t_1 \tag{2.51} $$

but also

$$ D^{(2)}_{t_1t_2d} = {}_D\overline{K}^{(2)}_{dt_1t_2} \qquad \text{and} \qquad D^{(2)}_{t_{12}t_2d} = {}_D\overline{K}^{(2)}_{dt_1t_2} \qquad \text{for} \quad t_2 > t_1 \tag{2.52} $$

and

$$ D^{(2)}_{t_1t_2d} = 2\ {}_D\overline{K}^{(2)}_{dt_1t_2} \qquad \text{for} \quad t_2 = t_1 \tag{2.53} $$

The last remaining issue is the inversion of Eq. (2.30). No particular property arises from the flat and symmetric nature of the structure and thus a stronger assumption is necessary. To proceed, it was assumed here that

$$ {}_D K^{(3)}_{mpln} = {}_D K^{(3)}_{mlpn} \tag{2.54} $$

According to which

$$ {}_D K^{(3)}_{mnlp} = \begin{cases} {}_D\overline{K}^{(3)}_{mnnn} & \text{for} \quad p = l = n \\ \frac{1}{3}\ {}_D\overline{K}^{(3)}_{mlln} & \text{for} \quad p = l > n \\ \frac{1}{3}\ {}_D\overline{K}^{(3)}_{mpll} & \text{for} \quad p > l = n \\ \frac{1}{6}\ {}_D\overline{K}^{(3)}_{mnlp} & \text{for} \quad p > l > n \end{cases} \tag{2.55} $$

with other values obtained from the symmetries of Eqs (2.54) and (2.31). Then, from Eq. (2.32) and (2.47),

$$\overline{D}^{(3)}_{mlpn} = \begin{cases} 0 & \text{for } p < l \\ 2\ {}_D\overline{K}^{(3)}_{mnnn} & \text{for } p = l = n \\ \frac{2}{3}{}_D\overline{K}^{(3)}_{mnll} & \text{for } p = l > n \\ \frac{2}{3}{}_D\overline{K}^{(3)}_{mlln} & \text{for } p = l < n \\ \frac{4}{3}{}_D\overline{K}^{(3)}_{mllp} & \text{for } p > l = n \\ \frac{4}{3}{}_D\overline{K}^{(3)}_{mlpp} & \text{for } p = n > l \\ \frac{2}{3}{}_D\overline{K}^{(3)}_{mlnp} & \text{for } p > n > l \\ \frac{2}{3}{}_D\overline{K}^{(3)}_{mnlp} & \text{for } p > l > n \end{cases} \cdot \qquad (2.56)$$

3. THE GOLAND WING

3.1. Structural Model

The Goland wing will be used in the next Chapter to assess the effects of structural nonlinearities, from both proposed NSD and/or stiffness-related geometric nonlinearity. The Goland wing is a standard aeroelastic model, it is a rectangular wing of constant thickness, aspect ratio equal to 10, and exhibiting a tip store as shown in Figure 3.1.

The Nastran finite element model is composed of four nodes square plate elements (CQUAD Nastran elements), 2 rows of 10 such elements on top of the wing and a similar layout on its bottom. These elements are complemented by a grid of bar elements (CROD Nastran elements) aligned both spanwise and chordwise to model the stiffeners. Another set of such bars connect the top and bottom surfaces in addition to shear panels (CSHEAR Nastran elements) placed both along the span and the chord at each intersection of the plates elements. The Young's modulus and Poisson ratio were taken as 1.4976×10^9 and 0.3333 for all elements. The geometrical dimensions of the plate, rod, and shear elements are given in Table 3.1. Finally, the tip store has a mass of 22.498 slug and zero mass moments of inertia except the one along the span direction which equals 50.3396 slug ft^2. The store is connected to the tip of the wing by rigid connections (RBE3 Nastran element) at 6 nodes of the tip.

A linear modal analysis of the Goland wing (SOL 103 in Nastran) yielded the first natural frequencies given in Table 3.2 and the first five mode shapes shown in Figure 3.2-Figure 3.6. It is seen that the first mode is a spanwise bending more while mode 2 is the

first spanwise torsion. Moreover, while modes 1-4 are transverse, mode 5 is in-plane, it is a lead-lag mode.

Unless specified, a linear Rayleigh damping was assumed to represent the dissipation in the wing. The corresponding damping matrix of the full finite element model was expressed as

$$C_{lin} = \alpha M + \beta K^{(1)} \tag{3.1}$$

where M and $K^{(1)}$ are the finite element mass and linear stiffness matrices. The coefficients and were selected as $\alpha=2.565\text{x}10^{-1}$ s^{-1} and $\beta= 1.338\text{x}10^{-4}$ s which lead to damping ratios of 1.279%, 0.797%, 0.608%, 0.644% and 0.654% for the first five transverse modes.

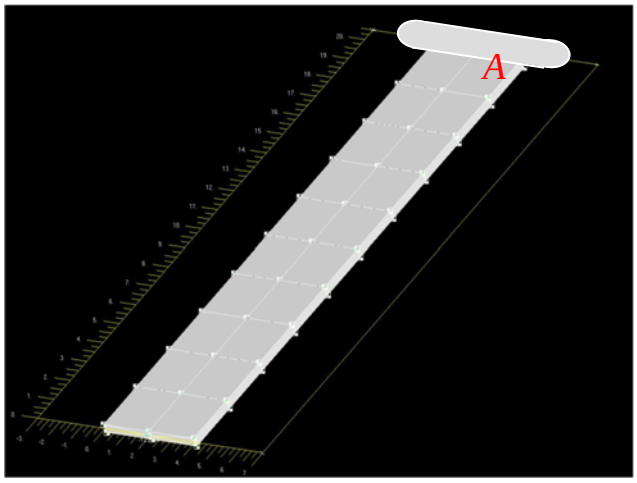

Figure 3.1. Goland Wing Structural Model

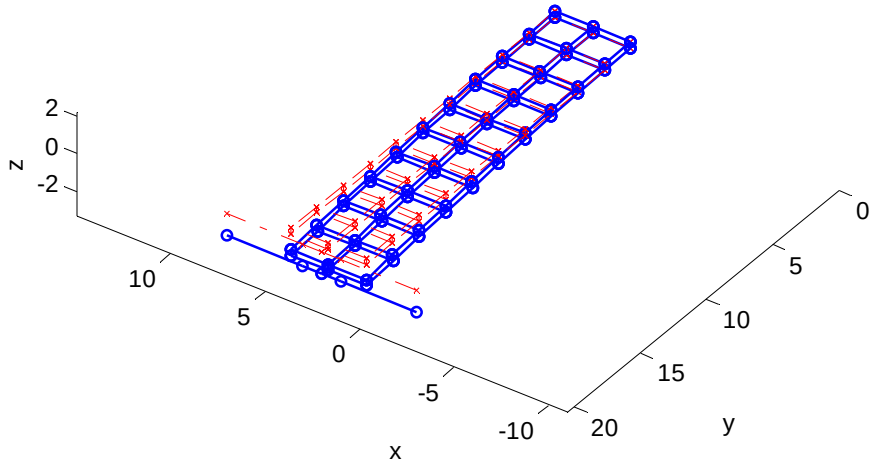

Figure 3.2. Linear Mode 1. Shown in Blue and Red Are the Deformed and Undeformed Wings.

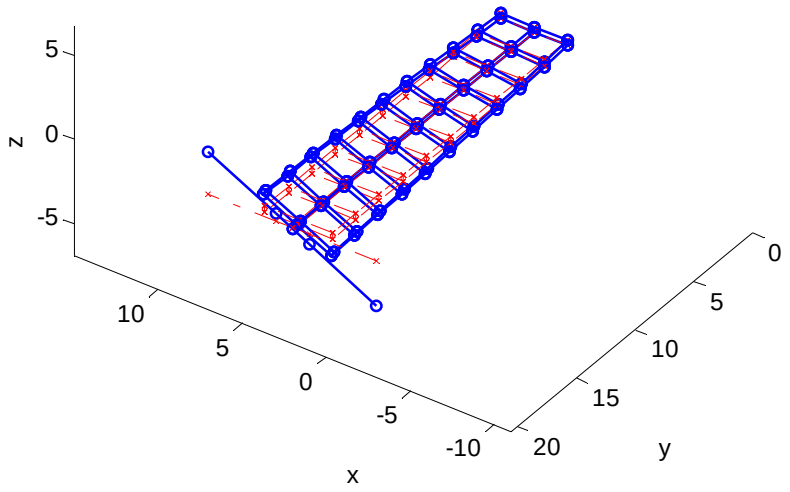

Figure 3.3. Linear Mode 2. Shown in Blue and Red Are the Deformed and Undeformed Wings.

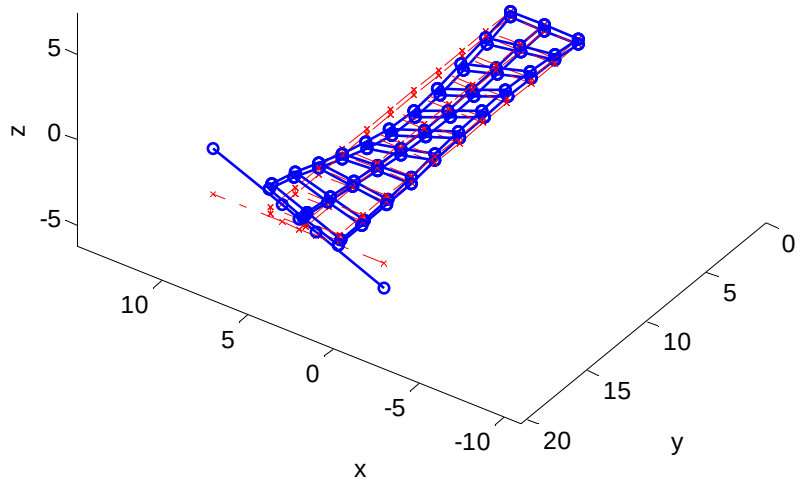

Figure 3.4. Linear Mode 3. Shown in Blue and Red Are the Deformed and Undeformed Wings.

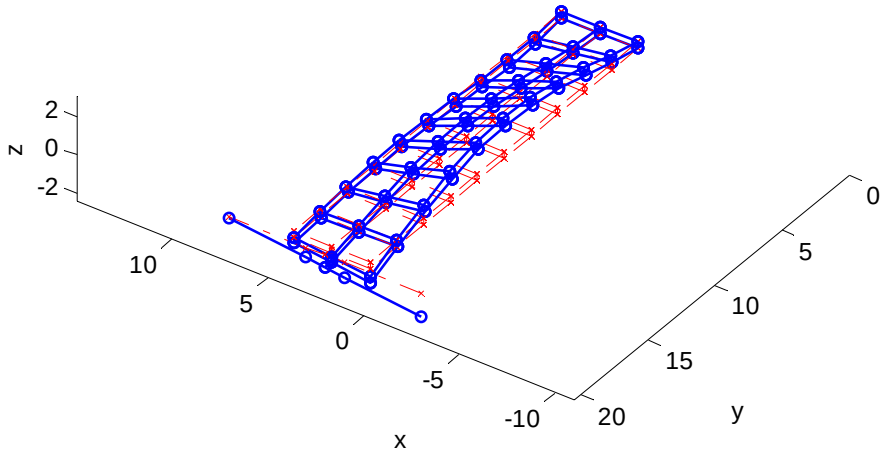

Figure 3.5. Linear Mode 4. Shown in Blue and Red Are the Deformed and Undeformed Wings.

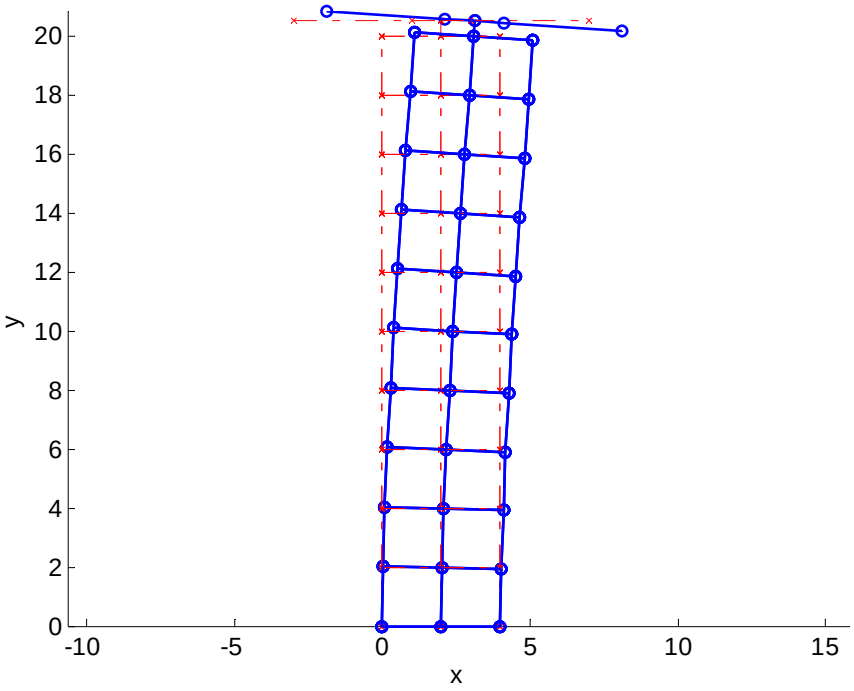

Figure 3.6. Linear Mode 5. Shown in Blue and Red Are the Deformed and Undeformed Wings.

Table 3.1. Dimensions of Finite Elements

Elements	Length (ft)	Width (ft)	Thickness (ft)
Plates	2	2	0.0155
Shear spanwise (mid-wing)	2	0.33334	0.0889
Shear spanwise (edges)	2	0.33334	$6x10^{-4}$
Shear chordwise	2	0.33334	0.0347
Rods	Length (ft)	Area (ft^2)	
Spanwise (mid-wing)	2	0.1496	
Spanwise (edges)	2	0.0416	
Chordwise	2	0.0422	
Thicknesswise	0.33334	$8x10^{-4}$	

Table 3.2. Natural Frequencies of the Goland Wing

Mode #	Nat. Freq. (Hz)	Mode #	Nat. Freq. (Hz)
1	1.690	6	16.260
2	3.051	7	22.845
3	9.172	8	26.318
4	10.834	9	29.183
5	11.258		

3.2. Aeroelastic Model

The modeling of the aerodynamic forces acting on the Goland wing during constant speed level flight was achieved in the modal domain, i.e., with the structural response expressed as in Eq. (2.8), using the ZONA Technology code ZAERO. The first step of the linear modeling process assumes a harmonic motion of the structure proportional to each structural mode in turn and determines the ensuing harmonic pressure field on the structure. This field is then integrated to yield the aerodynamic modal forces expressed as

$$\underline{F}_{Aero}(t) = -q_\infty \, Q(ik, M_\infty) \, \underline{q} \, e^{i\omega t} \tag{3.2}$$

where M_∞, V_∞, and q_∞ are the upstream Mach number, velocity, and dynamic pressure. Further, ω is the frequency of structural vibrations and *k* is the corresponding reduced frequency $k = \omega c / V_\infty$ where *c* is the half wing chord. Finally, $Q(ik, M_\infty)$ is the so-called matrix of generalized aerodynamic forces which is evaluated by ZAERO for user specified structural modes and reduced frequencies at a given Mach number.

The representation of the aerodynamic forces in the frequency domain as Eq. (3.2) is particular convenient for the steady state and flutter analyses of *linear* structures but nonlinear structural modes, such as those of Chapter 2, require a time-domain

representation of the aerodynamic forces. It can be obtained through a "rational function approximation" of the generalized aerodynamic forces as

$$Q(ik, M_\infty) = A_0 + A_1\, ik - A_2\, k^2 + ik\, D\left[ik\, I_{na} - R\right]^{-1} E \tag{3.3}$$

where A_0, A_1, A_2 are real *m*x*m* matrices. Further, *na* is the number of aerodynamic modes assumed and the real matrices *D*, *R*, and *E* are of respective dimensions *m*x*na*, *na*x*na*, and *na*x*m*. Finally, I_{na} denotes the *na*x*na* identity matrix.

Once the approximation of Eq. (3.3) is carried out (as part of ZAERO), the aerodynamic forces can be rewritten directly in terms of the structural generalized coordinates $\underline{q}(t)$ as

$$\underline{F}_{Aero}(t) = -\frac{q_\infty c^2}{V_\infty^2} A_2\, \ddot{\underline{q}} - \frac{q_\infty c}{V_\infty} A_1\, \dot{\underline{q}} - q_\infty A_0\, \underline{q} - q_\infty D \underline{\xi} \tag{3.4}$$

where the time-dependent variables $\underline{\xi}$ are referred to as the aerodynamic lag modes and satisfy the first order differential equations

$$\dot{\underline{\xi}} - E\, \dot{\underline{q}} - \frac{V_\infty}{c} R\, \underline{\xi} = \underline{0}\,. \tag{3.5}$$

Combining Eqs (3.4) and (3.5) with the structural equations of motion provides a complete modeling of the aeroelastic system. The selection of the number of lag modes and the assessment of the approximation of Eq. (3.3) can be validated by comparing the flutter conditions predicted by the frequency-domain (Eq. (3.2)) and time-domain (Eqs (3.4) and (3.5)) aeroelastic models.

The "*k*-method" was adopted in ZAERO to determine the frequency-domain flutter conditions. With the Mach number specified as M_∞ = 0.70, it remained to find the altitude

h and the flutter frequency ω. These quantities are determined so that the complex impedance matrix of the aeroelastic system

$$H_{Aero} = K^{(1)} + i\omega C_{lin} - M\,\omega^2 + q_\infty\, Q\left(i\frac{\omega c}{V_\infty}, M_\infty\right) \tag{3.6}$$

has a zero eigenvalue. The corresponding eigenvector is the flutter mode. Note that Eq. (3.6) must be complemented with tables of atmospheric properties providing the density ρ_∞ and speed of sound a_∞ in terms of altitude. Then,

$$V_\infty = M_\infty\, a_\infty \qquad \text{and} \qquad q_\infty = \frac{1}{2}\rho_\infty (2c) V_\infty^2 . \tag{3.7}$$

The prediction of the flutter altitude using the time-domain aerodynamic model was carried out by a trial and error process in which the altitude was specified at a particular value, the wing perturbed from rest at $t = 0$, and its equations of motion subjected to the forces of Eq. (3.4) marched in time (using a Newmark-β algorithm with a time step of 10^{-3} s). If the response was observed to decay (resp. increase) with time, the altitude was decreased (resp. increased) until a nearly stable response was observed. The frequency ω could then be estimated from the structural response.

The two methods gave close agreement with *na* = 13 aerodynamic lag modes leading to a flutter altitude of 11500 ft and a frequency of 1.972Hz. As could be expected, it was found that the flutter mode involved primarily the first bending and first torsion linear modes and, in fact, mostly the first bending as can be confirmed by the closeness of the flutter frequency with the natural frequency of the first mode. See Table 3.3 for the flutter frequencies at different altitudes.

Table 3.3. Flutter Frequencies at Different Altitude

Altitude (ft)	4000	6000	8000	10000	11000
Frequency (Hz)	1.851	1.881	1.911	1.945	1.962

3.3. Dissipation Modeling

To complete the characterization of the Goland wing, it remains to specify a dissipation tensor that will be used as a basis for the nonlinear structural damping model. Through the specification of a Young's modulus and Poisson ratio, it has effectively been assumed that the material is isotropic and homogenous from the elasticity tensor standpoint. Then, the dissipation tensor will be assumed to exhibit the same properties. Further, since the identification of the nonlinear damping parameters will be accomplished through a parallel with stiffness properties, the dissipation will be characterized by "equivalent" Young's modulus E_D and Poisson ratio ν_D. That is,

$$D_{ijkl} = \lambda_d \, \delta_{ij} \delta_{kl} + \mu_d \left(\delta_{ik} \delta_{jl} + \delta_{il} \delta_{jk} \right) \tag{3.8}$$

with

$$\mu_d = \frac{E_D}{2(1+\nu_D)} \qquad \text{and} \qquad \lambda_d = \frac{E_D \, \nu_D}{(1+\nu_D)(1-2\nu_D)}. \tag{3.9}$$

Note that E and E_D do not have the same units.

4. RESULTS

4.1. Chapter Overview

This chapter provides the results of the post-flutter aeroelastic analysis of the Goland wing of Chapter 3 subjected to nonlinear geometric effects in either damping and/or stiffness as modeled by the ROM of Chapter 2. The first step in this analysis, described in section 4.2, is the construction and validation of the ROM as a close approximation of the underlying full finite element, see sections 3.1 and 3.3. With this validated ROM, the post-flutter analysis of the Goland wing proceed in steps with linear stiffness and nonlinear damping in section 4.3, nonlinear stiffness and linear damping in section 4.4, and finally nonlinear stiffness and nonlinear damping in section 4.4.

4.2. ROM Construction and Validation

The construction of the reduced order model involves (i) the selection of basis functions that permit a good representation of the response, (ii) the identification of the stiffness and damping parameters, and (iii) the validation of the ROM with full finite element results on some particular loading. These steps are described in the ensuing sections.

4.2.1 Basis Functions - Dual modes

The primary component of the basis functions used to represent the motion of the wing are the lowest frequency linear modes, see section 3.1, and the first 9 were selected here focusing on a frequency band of interest of [0, 30] Hz. It is however recognized (Mignolet et al 2013) that these modes are not sufficient as they typically do not accurately capture

the “membrane” (in-plane) motions that occur in large displacements. This observation has led to the introduction of the “dual” modes to complement the basis (Kim et al 2013). These modes are constructed to capture the displacements not represented by the linear modes when these modes are excited. To this end, a series of loadings to the full finite element model are first determined that would induce in the linear case displacement fields that are exactly linear combinations of 1 or 2 linear modes. The nodal forces, denoted as $\underline{F}_{FE}^{(m)}$ for the loading case *m*, are of the form

$$\underline{F}_{FE}^{(m)} = \alpha_j^{(m)} \, \underline{\underline{K}}_{FE}^{(1)} \, \underline{\psi}^{(j)} \tag{4.1}$$

and

$$\underline{F}_{FE}^{(m)} = \alpha_j^{(m)} \, \underline{\underline{K}}_{FE}^{(1)} \, \underline{\psi}^{(j)} + \alpha_l^{(m)} \, \underline{\underline{K}}_{FE}^{(1)} \, \underline{\psi}^{(l)} \tag{4.2}$$

to induce displacements only along mode *j* only, Eq. (4.1), or modes *j* and *l* only, Eq. (4.2), in the linear case. In these equations, $\underline{\underline{K}}_{FE}^{(1)}$ is the global stiffness matrix of the finite element model and $\underline{\psi}^{(j)}$ is the *j*th linear mode.

When the forces of Eqs (4.1) and (4.2) are applied statically to the nonlinear finite element model, the computed displacements are no longer exactly linear combinations of the linear modes and the out-of-basis components, or residuals, of these displacements fields provide the raw data for the extension of the basis. More specifically, the dual modes are obtained through a proper orthogonal decomposition of the ensemble of residuals.

In the present effort, 12 values of the scaling factors $\alpha_j^{(m)}$ were used for each combination of modes, i.e., ±100, ±290, ±430, ±520, ±660, and ±800. They induce tip transverse displacements of the wing ranging from 1% to 15% of span.

The combinations of modes, i.e., the values of j and l, were chosen capture a broad range of expected motions. Since the flutter involves primarily modes 1 and 2, the combinations focused on those two modes and possible contributions of the three next ones. That is, the combinations considered were (j,l) =(1,1), (1,2), (1,3), (1,4), (1,5), (2,2), (2,3), (2,4), and (2,5). The proper orthogonal decomposition approach led to 9 dominant eigenvectors selected as dual modes and added to the 9 linear modes to form the basis. The first four dual modes are plotted in Figure 4.1 to Figure 4.4.

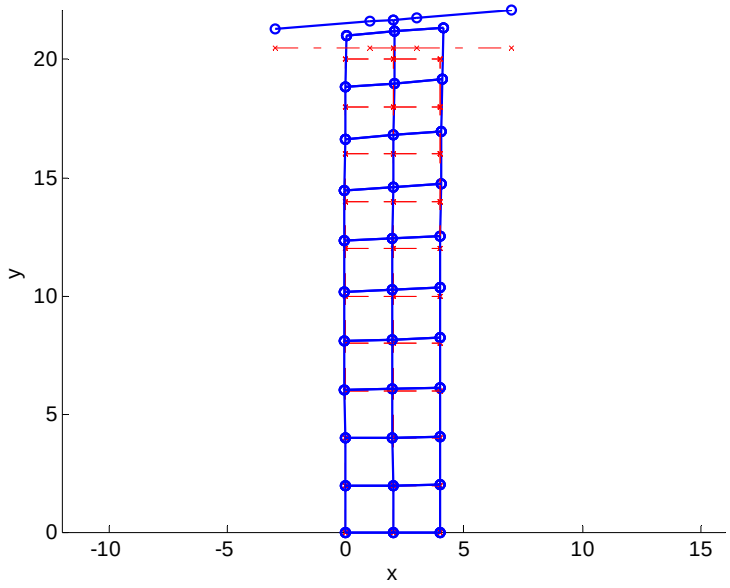

Figure 4.1. Dual Mode 1. Shown in Blue and Red Are the Deformed and Undeformed Wings.

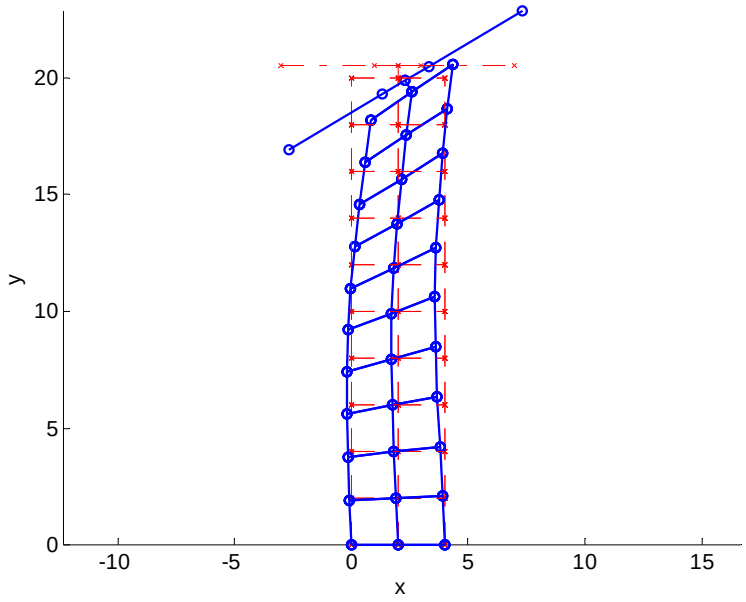

Figure 4.2. Dual Mode 2. Shown in Blue and Red Are the Deformed and Undeformed Wings.

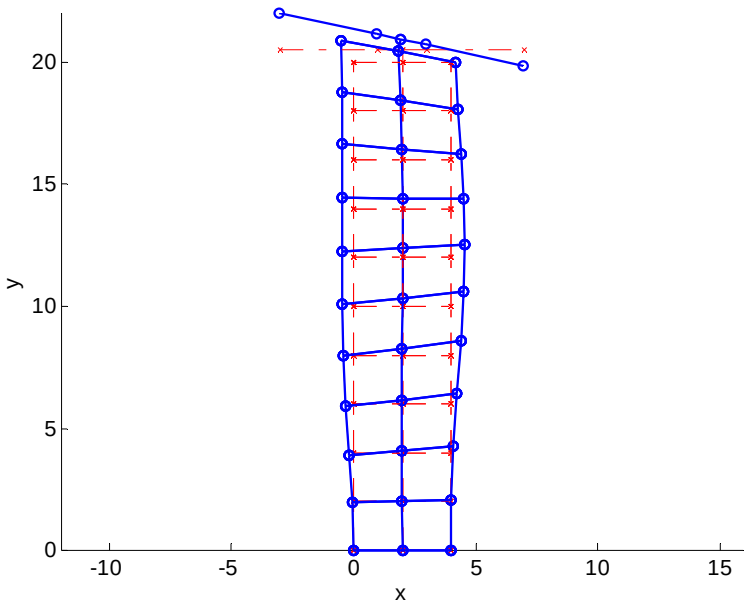

Figure 4.3. Dual Mode 3. Shown in Blue and Red Are the Deformed and Undeformed Wings.

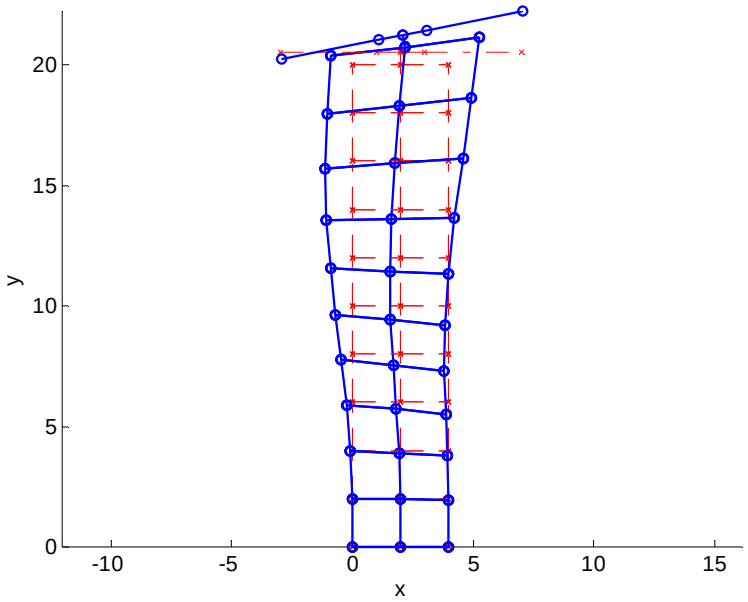

Figure 4.4. Dual Mode 4. Shown in Blue and Red Are the Deformed and Undeformed Wings.

4.2.2 Identification of Stiffness and Damping Parameters

The identification of the stiffness and damping parameters was carried out as described in section 2.3. For these computations, the scaling parameters q_j were selected to be 0.01 for all linear modes and 0.001 for the duals.

Within Nastran, the imposition of the displacement fields has usually been done using the DMAP Alter sequence written by A.A. Muravyov and S.A. Rizzi. This procedure is very efficient especially when there are a large number of load cases as it inserts the desired displacement field directly in the appropriate memory location at the appropriate stage of the computations. Although this alter sequence has worked on a large number of structures with a broad variety of elements, it led to incorrect linear stiffness terms for the Goland Wing model. This issue was identified to be linked to the CSHEAR elements in the model.

To resolve this issue, the displacement fields were applied to the model using single point displacement constraints (SPCD cards). Specifically, all nodes in the model were constrained except for a fictitious node whose purpose was to trigger the Nastran computations. Then, the constraint forces were outputted and processed as described in section 2.3. The linear stiffness coefficients found in this manner did indeed match those expected and the validation of the following section further confirmed the validity of the identified model. Note that the use of SPCD cards implied that Nastran proceeded through a full convergence analysis for each imposed displacement field. This process was significantly slower than using the DMAP alter but also required the selection of a convergence criterion selected here as 10^{-8} on displacements, 10^{-3} on forces, and 10^{-7} on energy.

4.2.3 Static Validation

A series of static validations were carried out to test the accuracy of the constructed ROM in comparison to the full finite element model. The first such validation focused on a uniform pressure in the transverse direction. A series of different load cases with different pressure magnitudes were used. Shown in Figure 4.5 to Figure 4.7 are the responses of node *A* in Figure 3.1. It is observed that the maximum difference in transverse displacement between the results from the ROM and the nonlinear Nastran computations ("SOL 106") is about 2%. Comparing the in-plane displacements, it is seen that the maximum difference in the dominant, spanwise direction is 5.6% but much larger for the chordwise displacement which is however two orders of magnitude smaller than the spanwise one. Since flutter is associated with the transverse wing deflections, this matching is considered

appropriate. Comparing the linear and nonlinear Nastran results, it appears that the wing does not seem to stiffen in the transverse direction, the dominant effect of geometric nonlinearity is seen here as the much larger spanwise deflection well captured by the ROM.

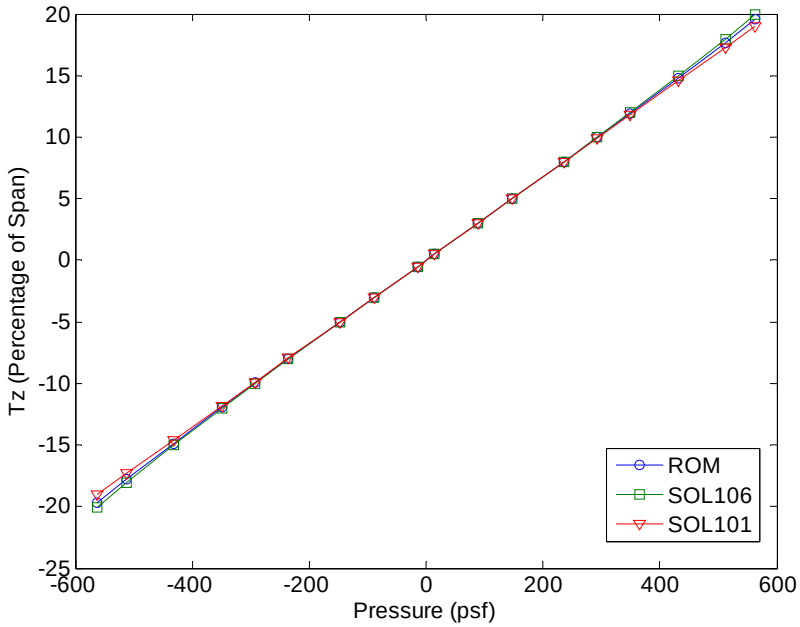

Figure 4.5. Transverse (Tz) Static Displacements at Node *A* under a Uniform Pressure, ROM and Nastran Nonlinear ("Sol 106") and Linear ("Sol 101") Solutions.

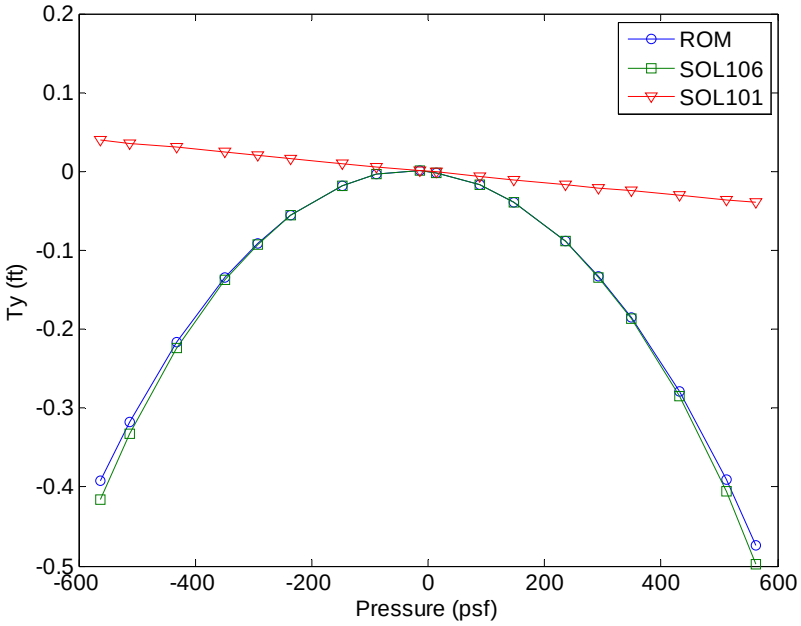

Figure 4.6. Spanwise (T_y) Static Displacements at Node *A* under a Uniform Pressure, ROM and Nastran Nonlinear ("Sol 106") and Linear ("Sol 101") Solutions.

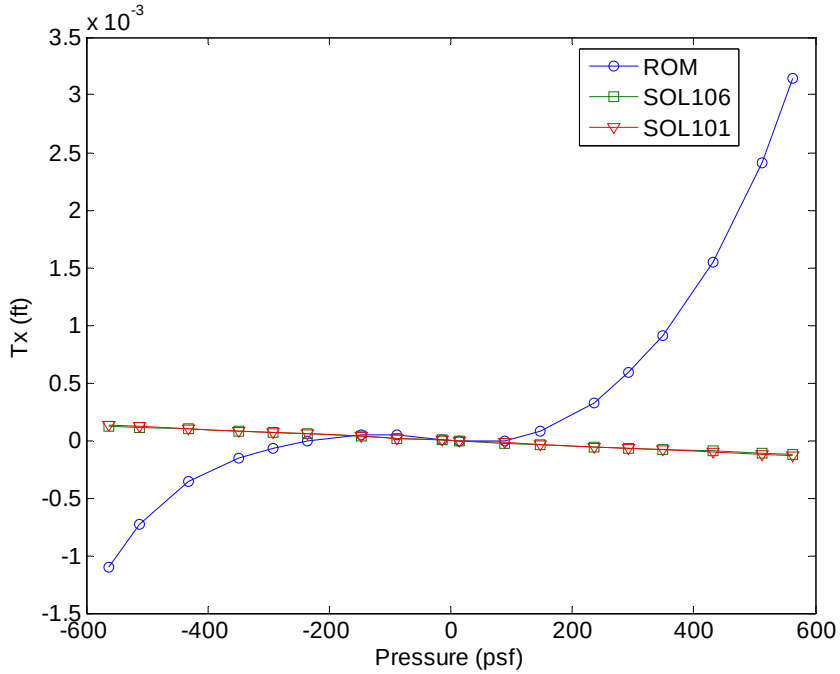

Figure 4.7. Chordwise (T_x) Static Displacements at Node *A* under a Uniform Pressure, ROM and Nastran Nonlinear ("Sol 106") and Linear ("Sol 101") Solutions.

A second validation was carried out with a non-uniform pressure in the transverse direction, defined to be zero at the root of the wing and linearly increasing until the tip. The comparisons of ROM and Nastran predictions for the same node are shown in Figure 4.8 to Figure 4.10 and a very similar to those shown in Figure 4.5 to Figure 4.7: the maximum difference between the ROM and SOL106 is 2.5% and 7.2% in the transverse and spanwise directions and, as before, the chordwise displacements are not correctly captured by the ROM. Again, note that the nonlinear geometric effects are most significant in the spanwise direction.

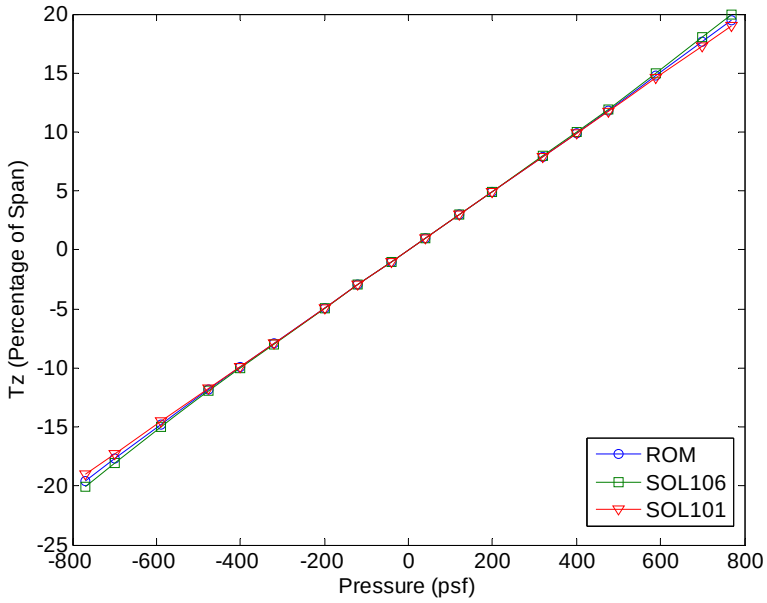

Figure 4.8. Transverse (T_z) Static Displacements at Node *A* under a Root-Tip Linear Pressure, ROM and Nastran Nonlinear ("Sol 106") and Linear ("Sol 101") Solutions.

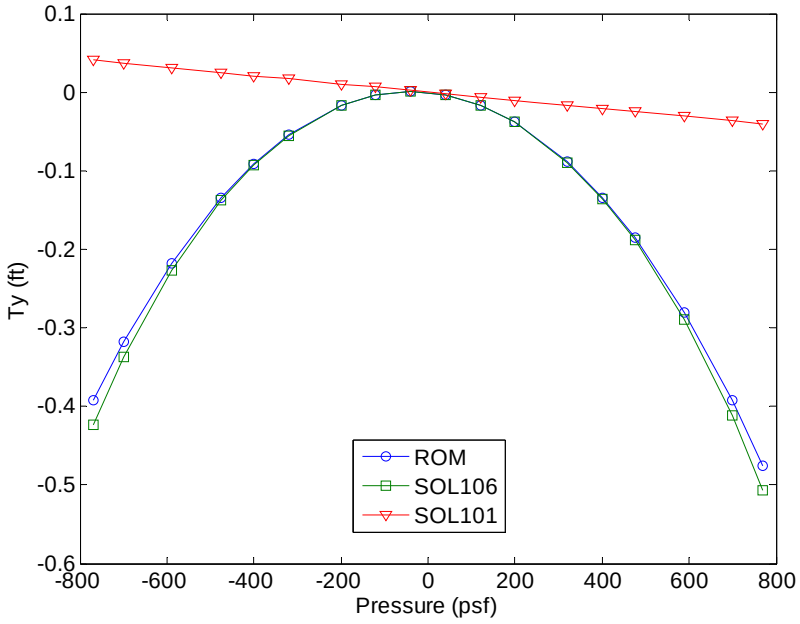

Figure 4.9. Spanwise (T_y) Static Displacements at Node *A* under a Root-Tip Linear Pressure, ROM and Nastran Nonlinear ("Sol 106") and Linear ("Sol 101") Solutions.

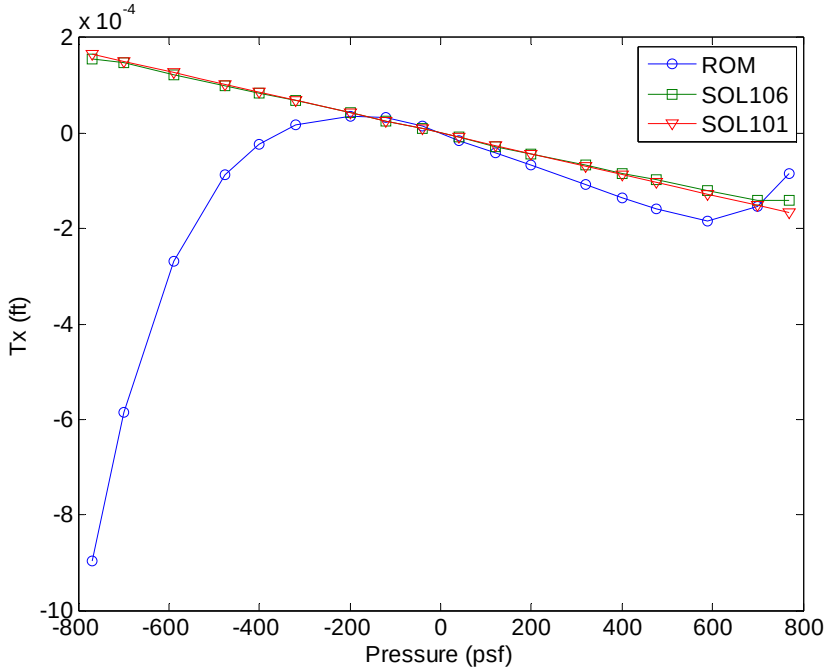

Figure 4.10. Chordwise (T_x) Static Displacements at Node *A* under a Root-Tip Linear Pressure, ROM and Nastran Nonlinear ("Sol 106") and Linear ("Sol 101") Solutions.

As flutter combines both bending and torsion motions, a third validation was performed with a torsional load applied to the structure. To this end, the pressure was defined to be zero along the mid line of the wing and varying linearly from leading to trailing edge, and constant along span. Shown in Figure 4.11 to Figure 4.13are the comparison of predicted displacements for the ROM and Nastran for the same node as before. It is observed that the maximum difference in the transverse direction between the ROM and SOL106 is around 11%. So the torsional motion is not captured as well as the bending ones of the previous validations. In this context, note that the stiffening of the wing in large displacements is now very clear and is mostly appropriately captured by the ROM.

To perform a validation in conditions as close as possible to flutter, a combination of the bending and torsion type loading of cases 1 and 3 was envisioned. In this regard, it was noted that the ratio of the amplitudes of the bending (first) and the torsional (second) modes in the flutter mode is about 15.5. Thus, in the final static validation, the pressure was selected as a combination of a uniform one and one varying linearly from leading to trailing edge with a ratio of 15.5 between. The comparison of the displacements predicted by the ROM and by Nastran are shown Figure 4.14 to Figure 4.16 and is very similar to the one obtained in the first validation.

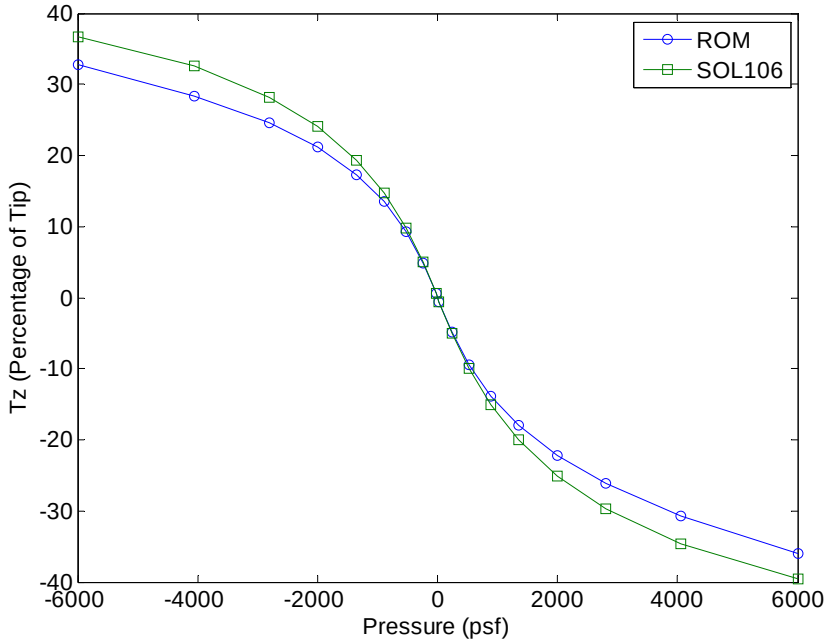

Figure 4.11. Transverse (T_z) Static Displacements at Node *A* under a Torsional Load, ROM and Nastran Nonlinear ("Sol 106") and Linear ("Sol 101") Solutions.

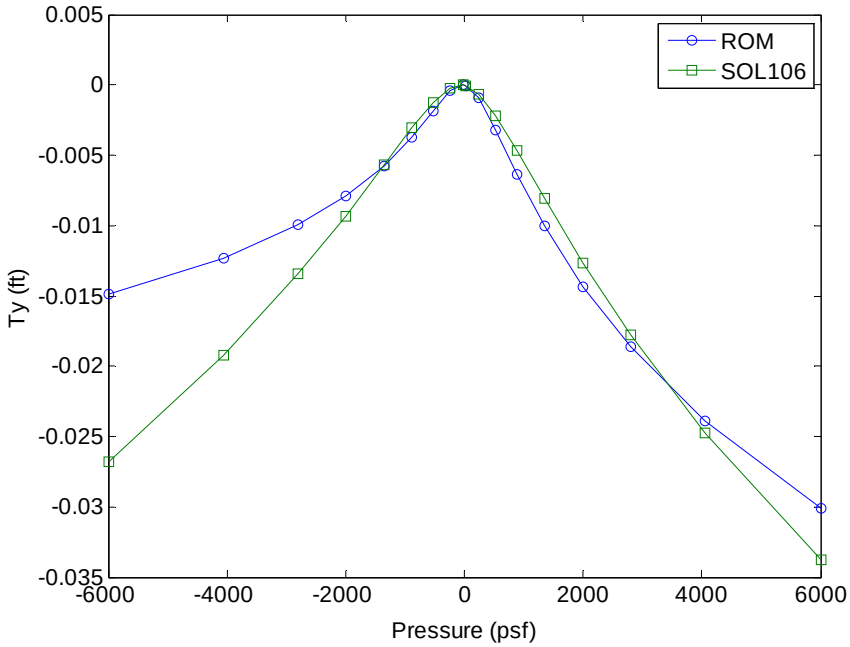

Figure 4.12. Spanwise (T_y) Static Displacements at Node *A* under a Torsional Load, ROM and Nastran Nonlinear ("Sol 106") and Linear ("Sol 101") Solutions.

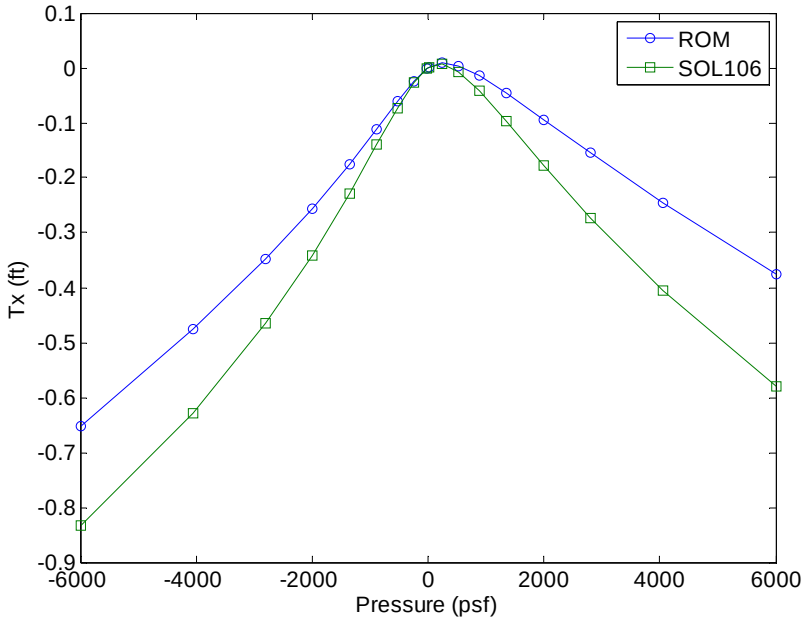

Figure 4.13. Chordwise (T_x) Static Displacements at Node *A* under a Torsional Load, ROM and Nastran Nonlinear ("Sol 106") and Linear ("Sol 101") Solutions.

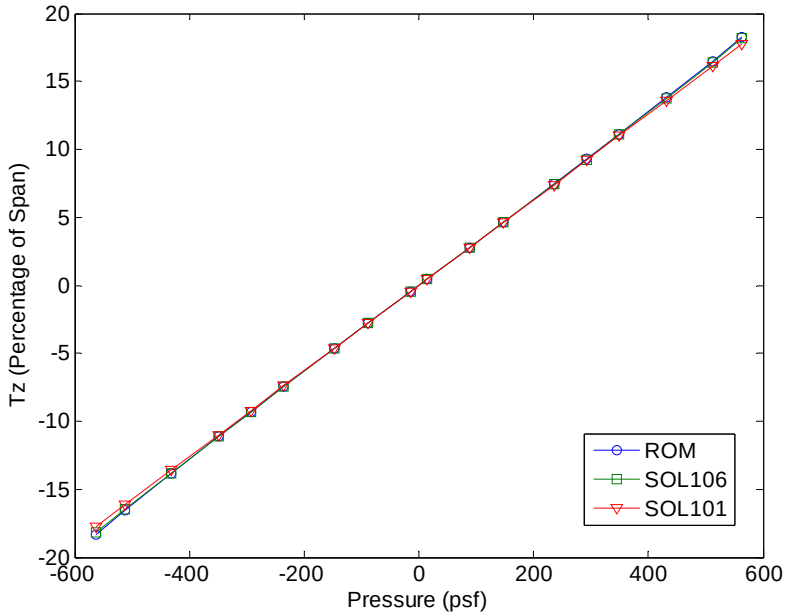

Figure 4.14. Transverse (T_z) Static Displacements at Node *A* under Combined Loading, ROM and Nastran Nonlinear ("Sol 106") and Linear ("Sol 101") Solutions.

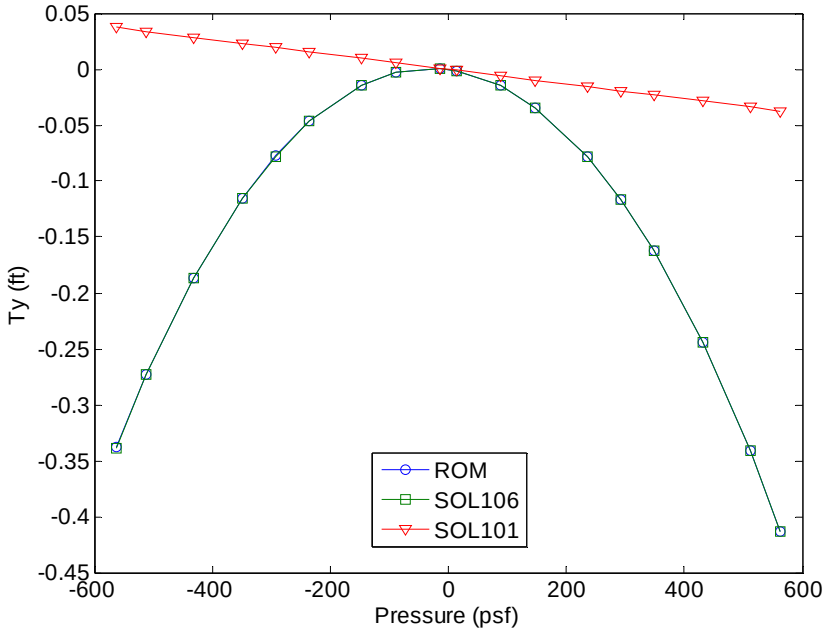

Figure 4.15. Spanwise (T_y) Static Displacements at Node *A* under Combined Loading, ROM and Nastran Nonlinear ("Sol 106") and Linear ("Sol 101") Solutions.

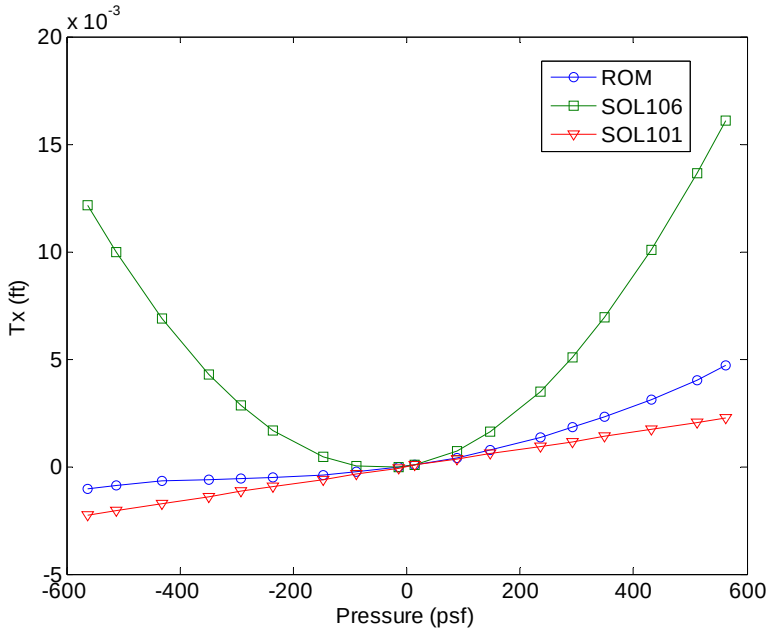

Figure 4.16. Chordwise (T_x) Static Displacements at Node *A* under Combined Loading, ROM and Nastran Nonlinear ("Sol 106") and Linear ("Sol 101") Solutions.

4.2.4 Dynamic Validation

The dynamic validation was intended to complement the static validations and, ideally, assess the closeness of the ROM predictions in comparison to their Nastran counterparts. However, possibly due to the CSHEAR elements in the model, convergence problems were constantly encountered in the NASTRAN computations, carried out here with the solution SOL400. Thus, only the dynamic response of the ROM is presented.

The loading was assumed to be a uniform pressure of magnitude varying in time as a zero mean Gaussian white noise in the band [0,200] Hz. The standard derivation of this white noise was selected to be either 100 or 1500 and the response was marched in time using a Newmark-β algorithm and a time step of $5x10^{-4}$ for 600000 time steps. The power spectral density of the responses at node *A* for these 2 loadings are shown in Figure 4.17 and Figure 4.18, and their means and standard derivations are given in Table 4.1 and Table 4.2.

The sharp peak of the power spectral density in the lower excitation case suggests that the response is close to linear and the observed first and third natural frequencies closely match those of Table 3.2. At the higher excitation level, the peaks are broader with the location of the first almost unchanged, consistently with the nearly linear behavior observed in Figure 4.5. The other modes however stiffen as can be seen from the increase of the peak frequencies.

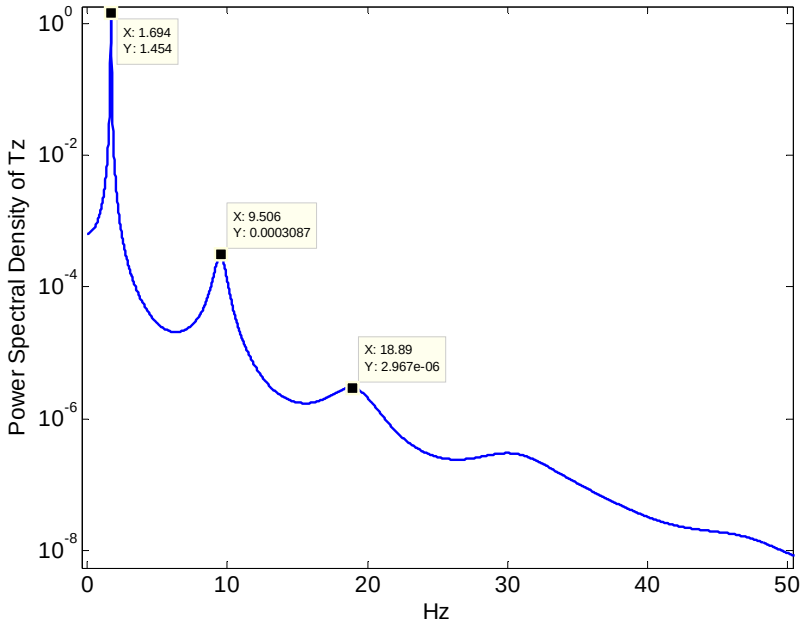

Figure 4.17. Power Spectral Density of the Transverse Displacement (T_z) of Node *A*, Dynamic Validation, Standard Deviation of 100.

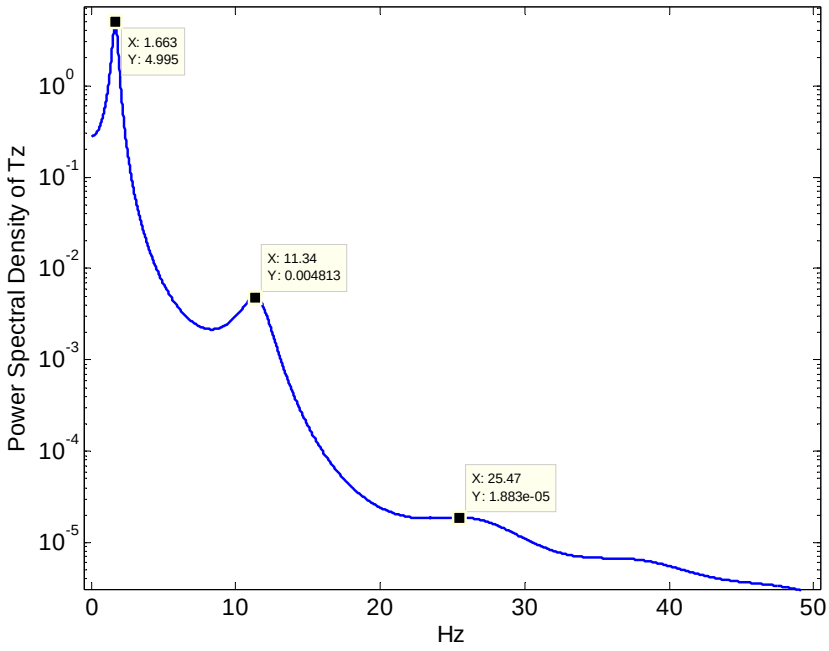

Figure 4.18. Power Spectral Density of the Transverse Displacement (T_z) of Node *A*, Dynamic Validation, Standard Deviation of 1500.

Table 4.1. Means and Standard Deviations of the Displacements of Node *A*, Dynamic Validation, Standard Deviation of 100.

	Chordwise (T_x)	Spanwise (T_y)	Transverse (T_z)
Mean (ft)	-1.602e-03	-2.588e-02	2.180e-04
Standard derivation (ft)	9.703e-03	4.237e-02	2.102

Table 4.2. Means and Standard Deviations of the Displacements of Node *A*, Dynamic Validation, Standard Deviation of 1500

	Chordwise (T_x)	Spanwise (T_y)	Transverse (T_z)
Mean (ft)	-2.242e-02	-9.404e-01	1.565e-02
Standard derivation (ft)	1.274e-01	1.134	1.260e+01

4.3. Post-Flutter LCO – Linear Stiffness/Nonlinear Damping

The previous section has provided a successful validation of the nonlinear reduced order model and in particular of its stiffness parameters. Since the parameters of the damping model will be obtained through a parallel with "equivalent" stiffness parameters (the pseudo stiffness parameters), it is expected that their identification will also be successfully achieved. Further, two cases were considered, one for which $\nu_D = 0$ and the other $\nu_D = 0.5$. Since the modulus E_D scales directly all damping parameters, only one value of this parameter was considered. For practical reasons (scaling of displacements involved in the identification), the damping parameters were estimated for $E_D = E$ and were then scaled for different values of E_D.

The linear damping matrix plays a particular role in the present analysis as it is the matrix used in predicting the flutter point, increasing it will lead to an increase of the flutter speed/decrease of the flutter altitude. Thus, in varying the parameters E_D and ν_D to assess the effects of the nonlinearity in damping, its linear counterpart should be held fixed. This approach would be consistent with practice since standard vibration testing methods would likely provide a good estimate of it. Then, the dissipation parameters E_D and ν_D will be used only to obtain quadratic and cubic damping coefficients. Note that, under this scheme, the positive definiteness of the tangent damping matrix $\underline{\underline{D}}^{(T)}$ is no longer guaranteed by Eq. (2.37).

The nonlinear damping with $\nu_D = 0$ was considered first and LCO was observed for a broad set of values of E_D for a series of altitudes as shown in Figure 4.19 and Figure 4.20, see Figure 4.21 for a typical time history and phase plane plot of the response of node *A*, the time history is plotted together with the flutter response at the same altitude. The amplitudes display the expected behavior: as the dissipation modulus E_D is increased, the amplitude of the response (and thus of the velocities) reduces to counteract the negative damping induced by the aerodynamics. Similarly, the amplitude of LCO increases with decreasing altitude, i.e., as this negative damping is increased. Note further that the LCO is seen to take place even at small fractions of the span, as seen for the F-16 and for which a linear stiffness assumption would seem valid.

The plot of the LCO frequency, Figure 4.20, shows clearly that this frequency is increasing slightly but consistently with increasing altitude and increasing value of E_D. Comparing these frequencies with their flutter counterparts, see Table 3.3, it appears that

the appearance of LCO at very value of E_D has led to a small drop in frequency, by about 1%-1.5%, at all altitudes. A change in frequency can be obtained by a change in the participation of the stiffer, second mode in the response and this is indeed what is observed, see Figure 4.22. This participation is increasing as a function of E_D consistently with the increase in frequency see in Figure 4.20. Further, the participation of the torsional mode at low values of E_D (around 17.5 at 8000ft) is smaller than for the flutter condition (about 12.5 at 8000ft) justifying the drop of frequency between flutter and LCO mentioned above. Note that the changes in the form of the response may, in addition to dissipation, affect the LCO occurrence and amplitude by altering the energy input from the aerodynamics. This issue will be discussed in more details in section 4.6.

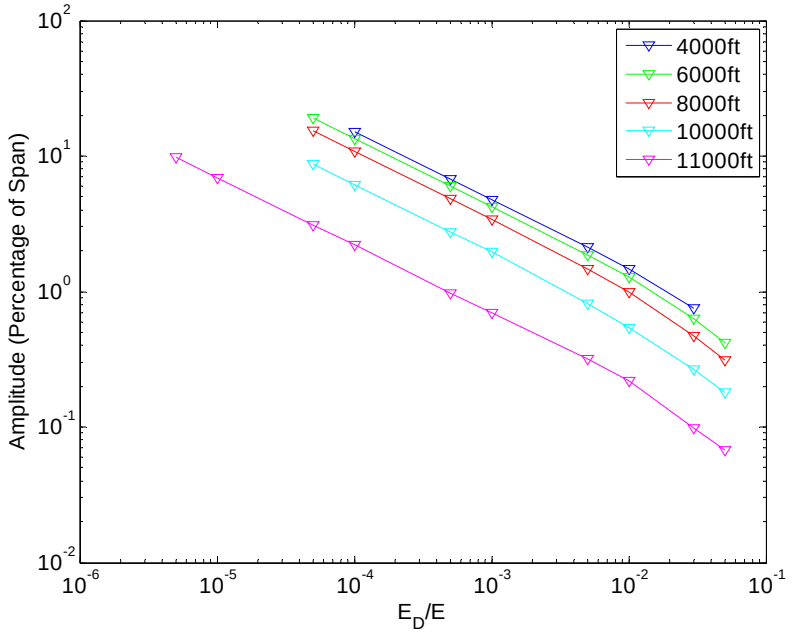

Figure 4.19. Amplitude of LCO as a Function of the Dissipation Modulus E_D for Various Altitudes, $\nu_D = 0$.

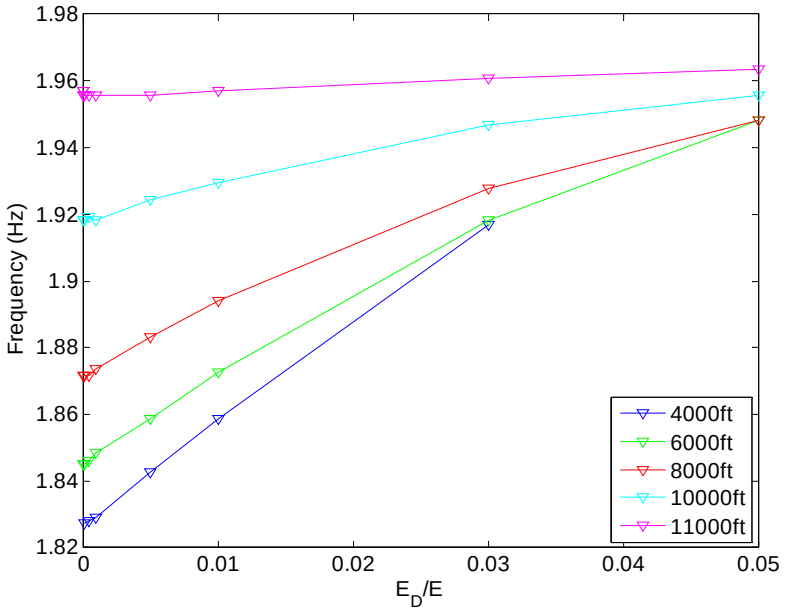

Figure 4.20. Frequency of LCO as a Function of the Dissipation Modulus E_D for Various Altitudes, $\nu_D = 0$.

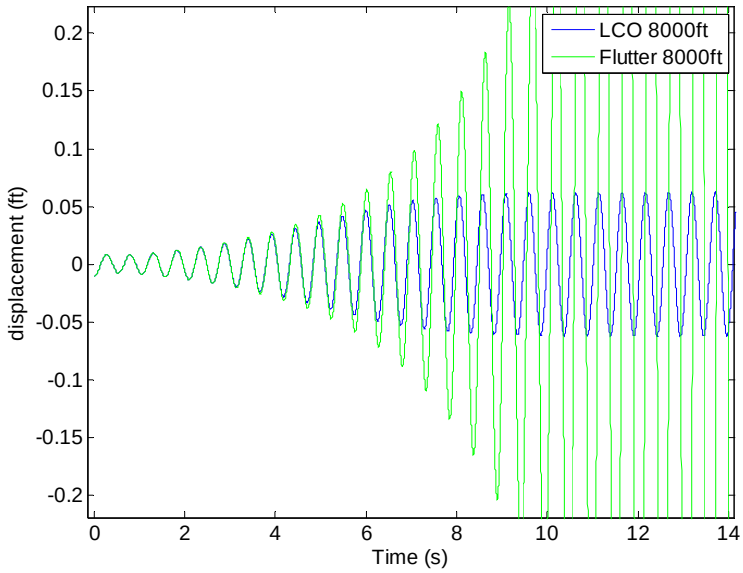

(a)

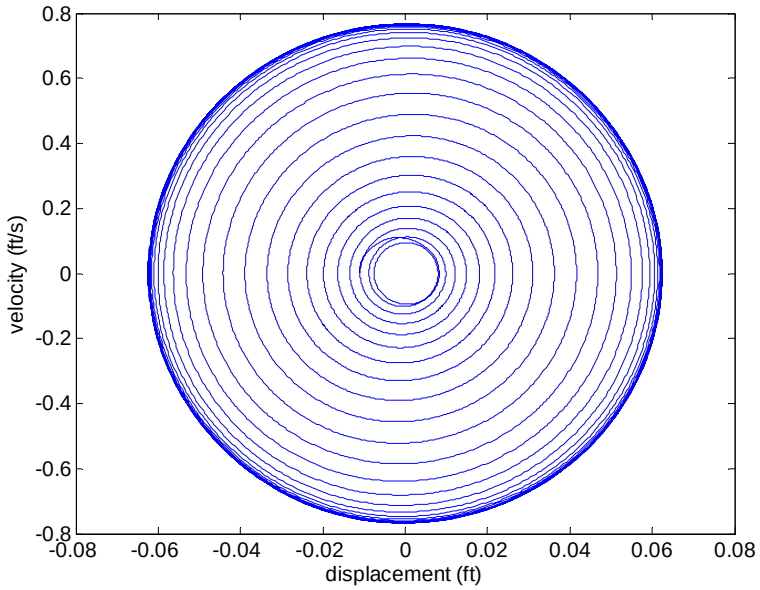

(b)

Figure 4.21. Transient Response of Node *A* toward LCO at 8000ft for E_D / E =0.05, ν_D = 0. (a) Time History of Transverse Displacement of Flutter and LCO; and (b) Corresponding Phase Plane Plot of LCO.

The plot of the LCO frequency, Figure 4.20, shows clearly that this frequency is increasing slightly but consistently with increasing altitude and increasing value of E_D. An increase in frequency can be obtained by an increased participation of the stiffer, second mode in the response and this is indeed what is observed, see Figure 4.22. This change in the form of the response may, in addition to dissipation, affect the LCO occurrence and amplitude by altering the energy input from the aerodynamics.

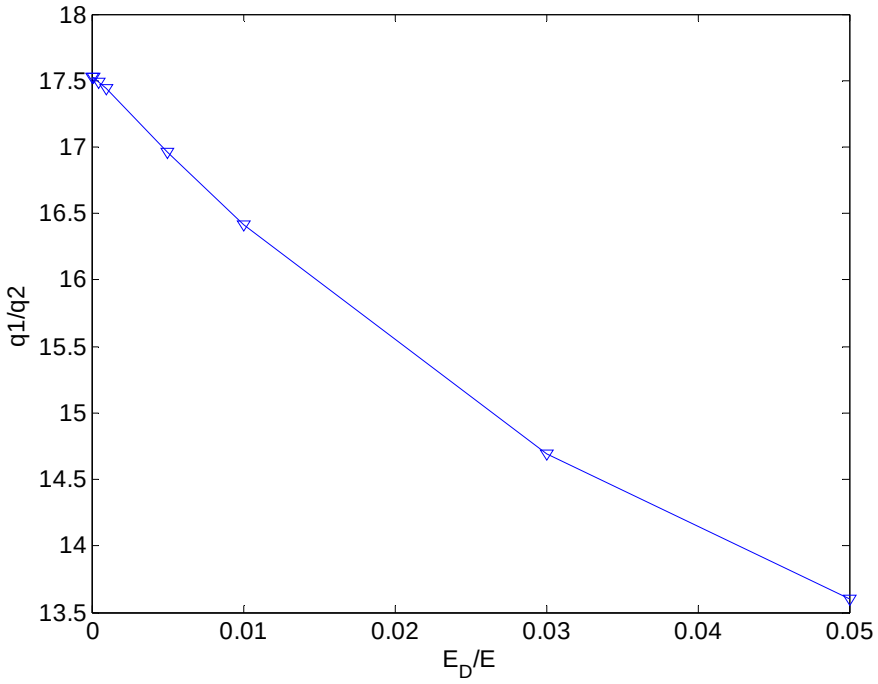

Figure 4.22. Ratio of Amplitudes of the First and Second Modes in the LCO Response, Altitude of 8000ft, $\nu_D = 0$

The coefficient ν_D was next selected equal to 0.5 and the analysis was repeated, see Figure 4.23 and Figure 4.24 for the LCO amplitude and frequency vs. the dissipation modulus E_D at different altitudes.

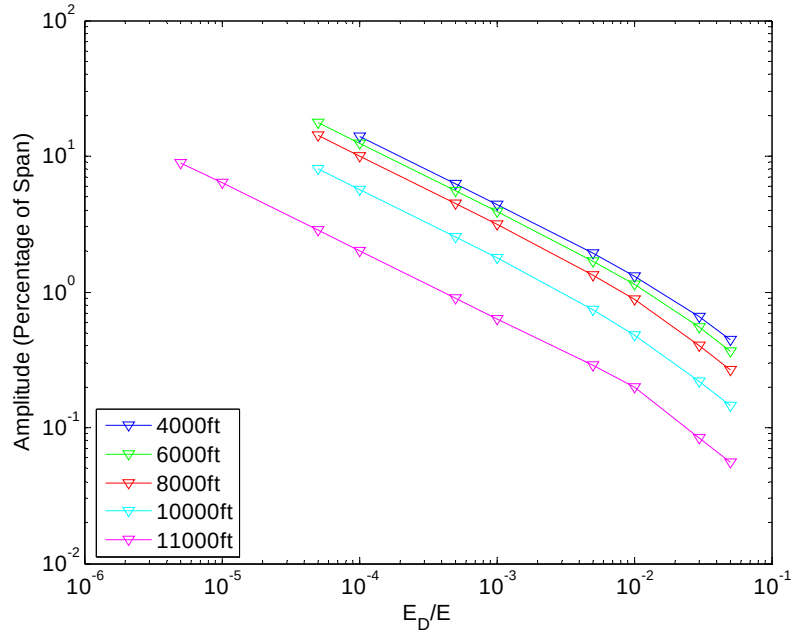

Figure 4.23. Amplitude of LCO as a Function of the Dissipation Modulus E_D for Various Altitudes, ν_D = 0.5.

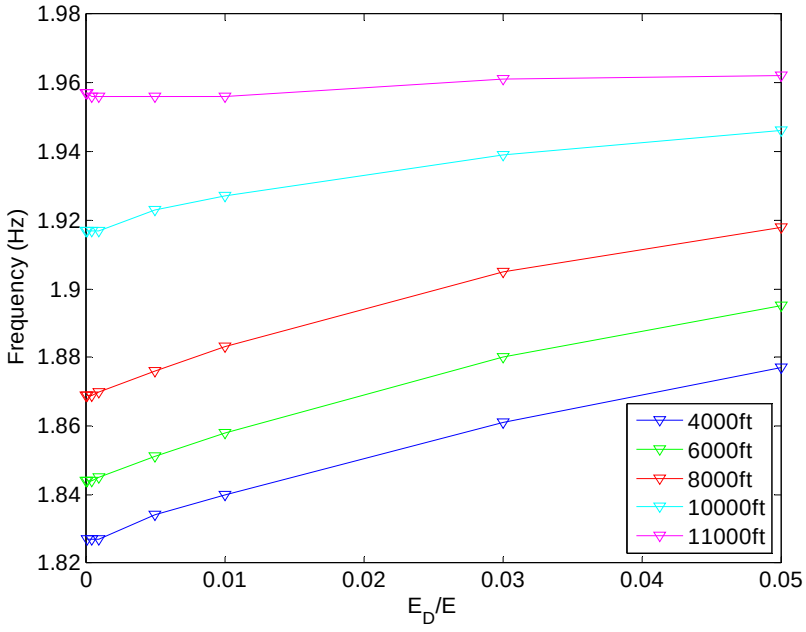

Figure 4.24. Frequency of LCO as a Function of the Dissipation Modulus E_D for Various Altitudes, ν_D = 0.5.

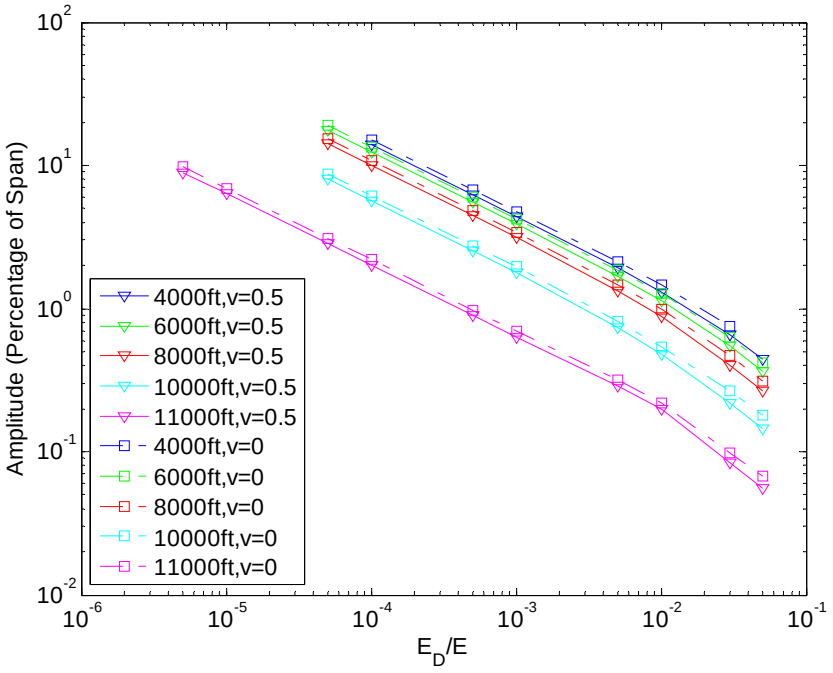

Figure 4.25. Comparison of Amplitude of LCO as a Function of the Dissipation Modulus E_D for Various Altitudes, ν_D = 0 and 0.5.

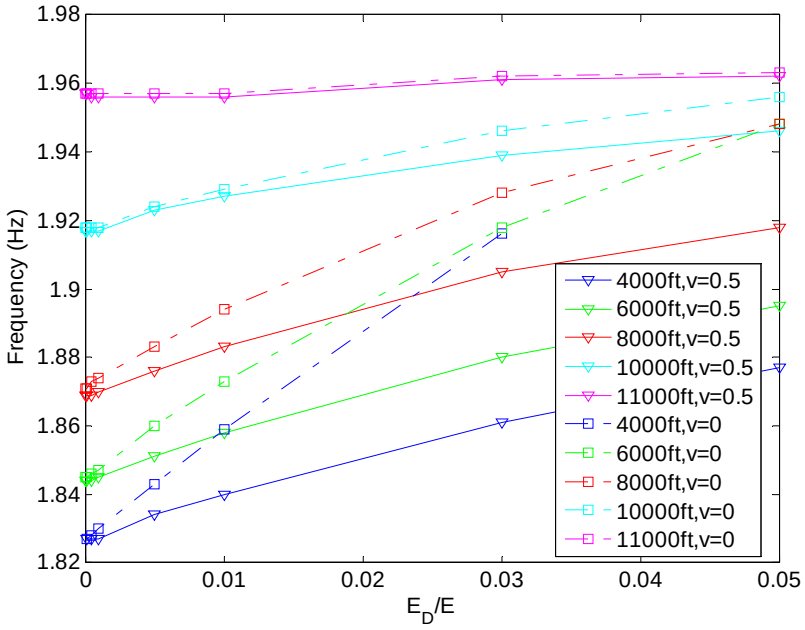

Figure 4.26. Comparison of Frequency of LCO as a Function of the Dissipation Modulus E_D for Various Altitudes, ν_D = 0 and 0.5.

The results obtained for ν_D = 0 and 0.5 appear very similar from Figure 4.19 and Figure 4.23 and Figure 4.20 and Figure 4.24 and thus to obtain a better comparison, they are plotted together on Figure 4.25 and Figure 4.26. From these figures, it appears that ν_D has very little effect on the amplitude of the LCO. Its effects on the frequency are more visible, possibly because the frequency changes are small. It appears that ν_D = 0 leads to a larger frequency increase, thus a larger presence of the torsional mode, but a slightly larger amplitude of LCO. These observations suggest that a decrease of the torsional mode would be beneficial to LCO maybe by reducing the interaction between the two modes which is a feature of wing flutter, see section 4.6 for discussion.

The above results were obtained with the 18-mode model including the first 9 linear and 9 dual modes. The latter are known to be required in the nonlinear geometric elastic case to capture the membrane stretching effects but it was questioned whether they need to be included here as nonlinear stiffness terms are not present. To assess this issue, the 18-mode model was truncated to eliminate the 9 dual modes and the LCO analysis was repeated. Then, shown in Figure 4.27 and Figure 4.28 are the LCO amplitudes and frequencies obtained with the two ROMs. It is seen that the amplitudes are very close to one another when they are “large”, larger than 1% of span say, but become increasingly different as the amplitude decreases/the dissipation modulus E_D increases. Interestingly, it is seen that the lower amplitude is achieved with the 18-mode model. It is suggested here that this model permits a transfer of energy from the linear modes to the dual ones where additional takes place leading to a reduction of the amplitude of response. Surprisingly, the plot of LCO frequencies, see Figure 4.28, indicates that they change only very slightly for the 9-mode model at the contrary of the 18-mode model.

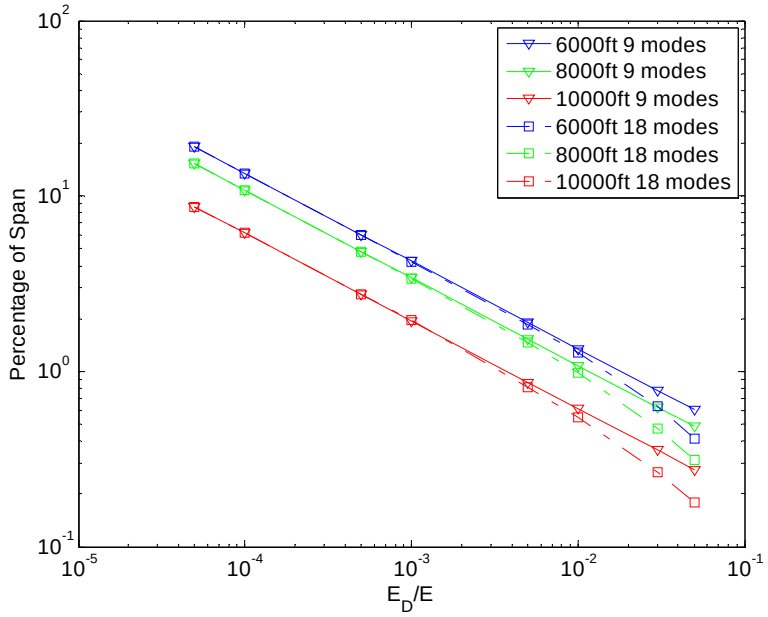

Figure 4.27. Comparison of Amplitude of LCO as a Function of the Dissipation Modulus E_D for Various Altitudes, ν_D = 0, 18-Mode and 9-Mode ROMs.

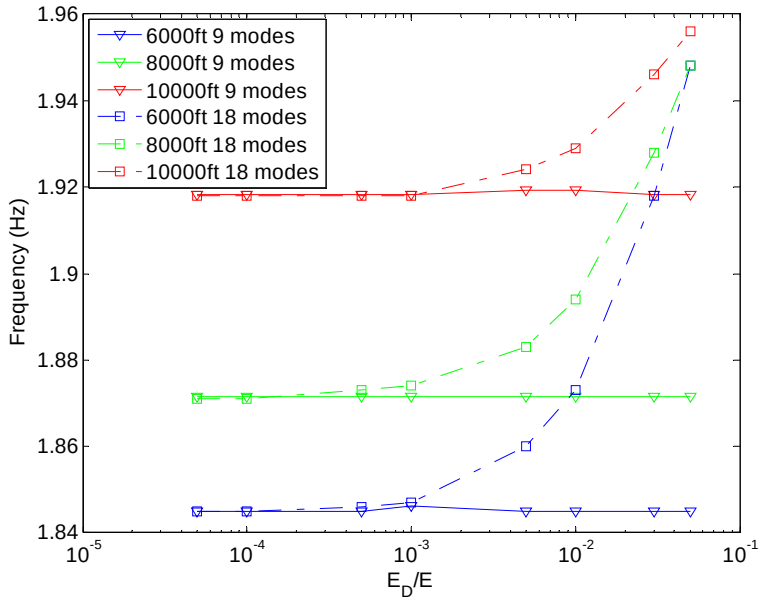

Figure 4.28. Comparison of Frequency of LCO as a Function of the Dissipation Modulus E_D for Various Altitudes, ν_D = 0, 18-Mode and 9-Mode ROMs.

It was stated at the beginning of this section that keeping the linear damping matrix did invalidate the proof of the positive definiteness of the tangent damping matrix. To assess this issue, an analysis of this matrix was carried over the entire cycle of response for an ensemble of the LCO solutions observed in Figure 4.19. Surprisingly, it was found that the tangent damping matrix of the 18-mode model exhibited some negative eigenvalues for E_D larger than typically 10^{-4} E, even though a finite amplitude LCO was observed. The eigenvectors associated with these negative eigenvalues were found to not correspond to physically occurring motions and thus do not lead to instability. Interestingly, the 9-mode model based on the linear modes only, and thus without any quadratic damping term, was found to have a positive definite tangent damping matrix in all solutions shown in Figure 4.27. Thus, although beneficial in the present situation, the transfer of energy from linear modes to dual modes through the quadratic damping terms appears to have the potential to induce instabilities when the linear stiffness matrix is retained. This issue will be revisited in section 4.5.

4.4. Post-Flutter LCO – Nonlinear Stiffness/Linear Damping

Limit cycle oscillations are expected to arise due to nonlinearities and, accordingly, it is questioned next whether they could happen from the nonlinear stiffness terms originating from the geometric nonlinearity alone. To assess this potential, the 18-mode ROM of section 4.2.4 with linear damping and nonlinear stiffness terms was coupled to the aerodynamics and responses computed. Limit cycle oscillations were indeed observed, see Table 4.3 and Table 4.4 for the amplitudes and frequencies for different altitudes. This finding may not have been obvious from the validation cases of section 4.2.3 and 4.2.4

which indicated a lack of stiffening, a possible softening in fact, of the first mode which is dominant in the flutter mode. Inspecting Table 4.4, it is seen that the frequency of LCO is larger than the one associated with flutter suggesting again an increase of the torsional mode component. Moreover, this mode does stiffen, see Figure 4.11. It is suggested that the combinations of these factors leads to the occurrence of LCO.

Table 4.3. Amplitude of LCO for Various Altitudes

Altitude (ft)	4000	6000	8000	10000	11000
Amplitude (ft)	1.3388	1.0773	0.7946	0.4502	0.1724

Table 4.4. Frequency of LCO for Various Altitudes

Altitude (ft)	4000	6000	8000	10000	11000
Frequency (Hz)	1.918	1.928	1.939	1.954	1.963

It is of interest to compare these results to those obtained with the nonlinear damping/linear stiffness model, see Figure 4.29 and Figure 4.30 for the results at 8000ft.

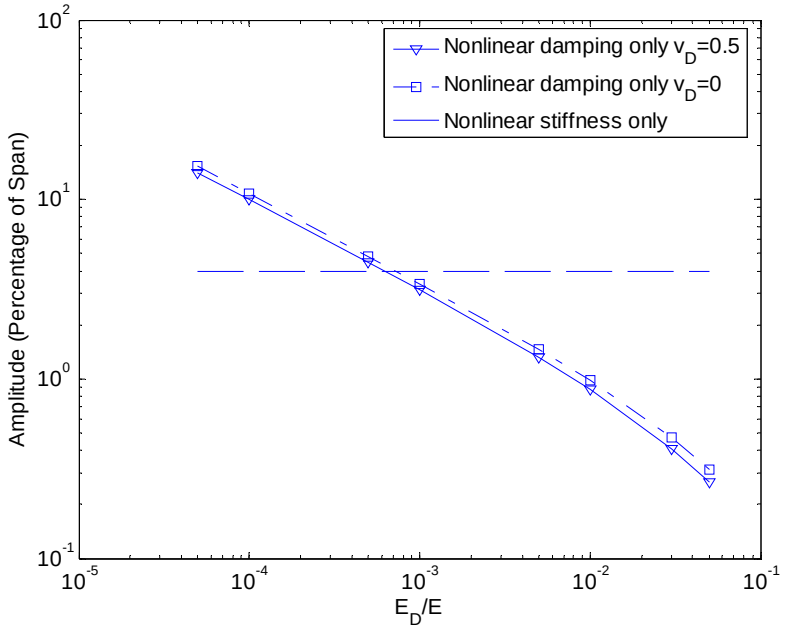

Figure 4.29. Comparison of Amplitude of LCO as a Function of the Dissipation Modulus E_D for Various Models at 8000ft.

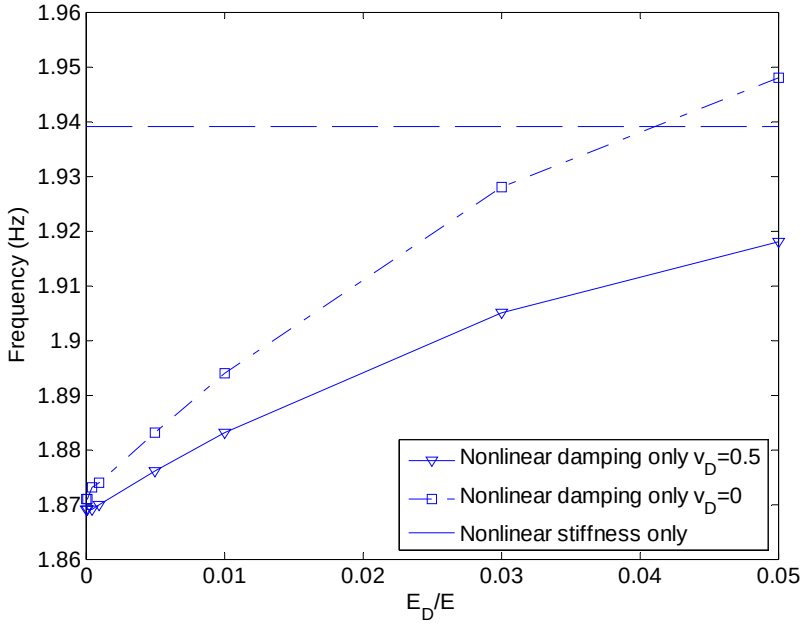

Figure 4.30. Comparison of Frequency of LCO as a Function of the Dissipation Modulus E_D for Various Models at 8000ft.

As expected, it is seen that the LCO amplitude obtained with nonlinear stiffness and linear damping intersects the curve of amplitude vs. dissipation modulus. For LCOs with larger amplitudes than this threshold, the nonlinear stiffness terms must absolutely be included in the analysis. For amplitudes much less than the threshold, it is likely that the nonlinear damping is the only significant structural nonlinearity.

4.5. Post-Flutter LCO – Nonlinear Stiffness/Nonlinear Damping

The results of the previous section suggest the need to include both nonlinear damping and nonlinear stiffness for LCO amplitudes that are of the order of 1 or a few percent of span. This final step of the effort requires the 18-mode model and was planned with nonlinear damping on all terms, i.e., with the quadratic damping terms included. However, the computations carried out with this model did not lead to LCO because the instability associated with the quadratic damping terms when the linear damping matrix is retained, see section 4.3 for discussion, became activated. Accordingly, the damping on the dual modes was eliminated but the nonlinear coupling with the quadratic stiffness terms was retained. This new model lead consistently to LCOs the amplitudes and frequencies of which are shown in Figure 4.31 and Figure 4.32. These results are also plotted on Figure 4.33 and Figure 4.34 with their counterpart with linear stiffness which are very close to those from Figure 4.27 and Figure 4.28 since there is then no coupling between linear and dual modes.

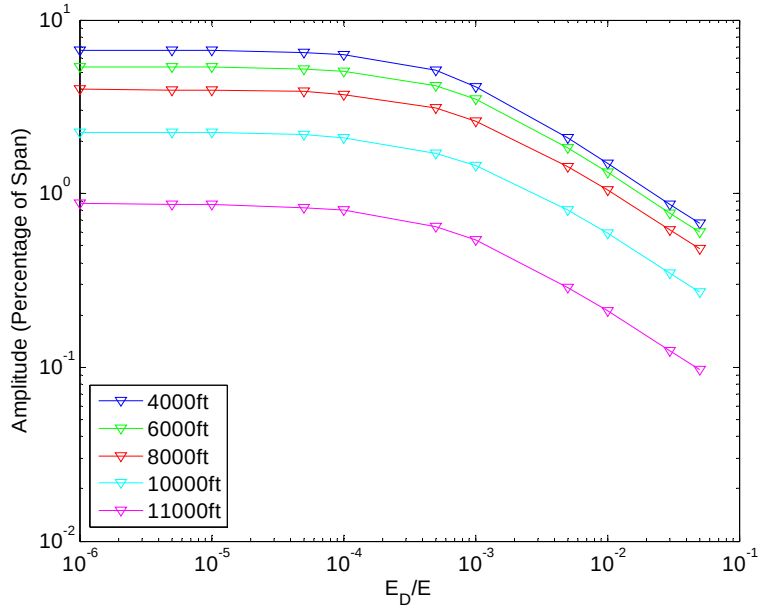

Figure 4.31. Amplitude of LCO as a Function of E_D for Various Altitudes, $\nu_D = 0$, Nonlinear Stiffness and Nonlinear Damping (on Linear Modes).

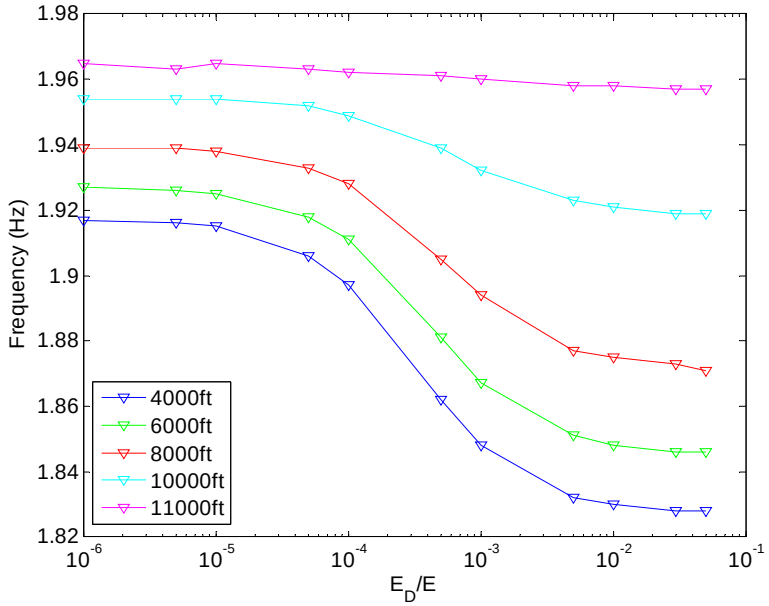

Figure 4.32. Frequency of LCO as a Function of E_D for Various Altitudes, $\nu_D = 0$, Nonlinear Stiffness and Nonlinear Damping (on Linear Modes).

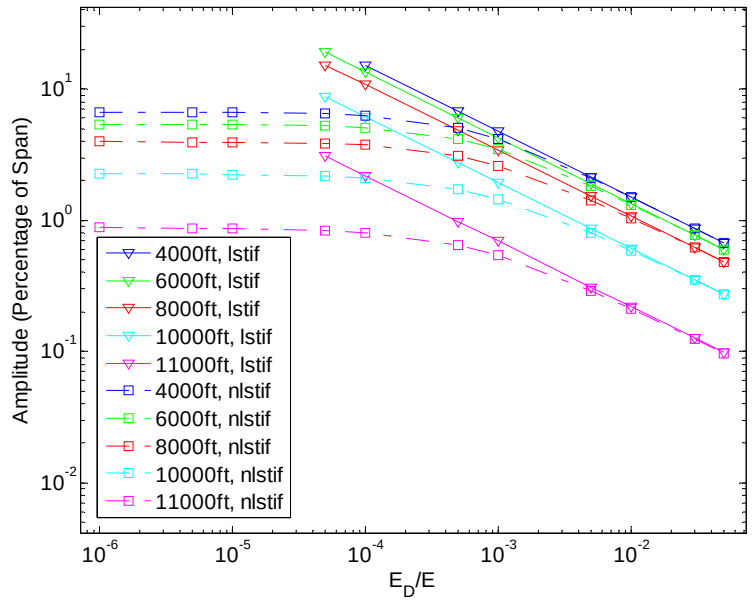

Figure 4.33. Comparison of Amplitude vs. E_D and Altitudes, ν_D = 0, Linear ("lstif") and Nonlinear Stiffness ("nlstif") with Nonlinear Damping (on Linear Modes Only).

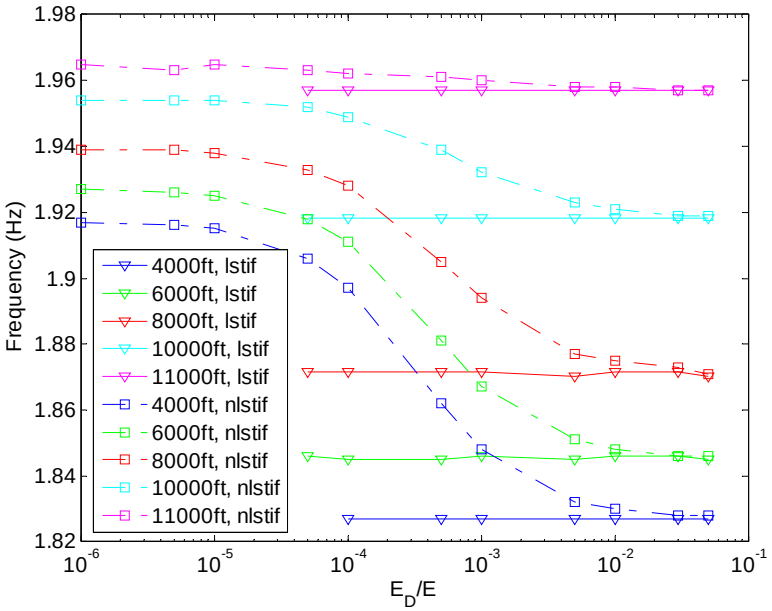

Figure 4.34. Comparison of Frequency vs. E_D and Altitudes, ν_D = 0, Linear ("lstif") and Nonlinear Stiffness ("nlstif") with Nonlinear Damping (on Linear Modes Only).

As expected, at low values of the dissipation modulus E_D, the nonlinear stiffness effects dominate the LCO and the results match closely those obtained with the linear damping matrix. As this modulus increases, dissipation becomes a more important bounding mechanism and the amplitude reduces to levels at which the nonlinear stiffness terms do not contribute significantly.

4.6. Nonlinear Damping – Aerodynamics Interaction

It was mentioned in Section 4.3 that the increased participation of the torsional mode observed with the 18-mode model, see Figure 4.22, could in turn modify the aerodynamics and thus have an effect on the magnitude of the resulting LCO. To assess this potential, the work input to the structure by the aerodynamics was evaluated for a series of conditions. Since the aerodynamic forces are linearly dependent on the structural deformations, it is expected that the work done by these forces over a cycle of motion would depend quadratically on the level of deformations. To this end, it is proposed here to analyze the normalized aerodynamic work per cycle defined as

$$\overline{W}_{aero} = \frac{\int_{t_0}^{t_0+2\pi/\omega} \underline{F}_{Aero} \cdot \dot{\underline{q}}\, dt}{\int_{t_0}^{t_0+2\pi/\omega} \underline{q} \cdot \underline{q}\, dt} \tag{4.3}$$

in which the denominator is introduced to normalize the work. In this equation, ω is the frequency of LCO (in rad/sec) and t_0 is an arbitrary time. Further, $\underline{F}_{Aero}$ are the aerodynamic forces of Eq. (3.4).

To validate the normalization factor in the denominator of Eq. (4.3), the response at

flutter (e.g., seen in green in Figure 4.21(a) for 8000ft) was first considered and the work $\overline{W}_{aero}$ was computed for the various altitudes and a series of consecutive cycles. Shown in Figure 4.35 is the evolution of $\overline{W}_{aero}$ as a function of the cycle number at different altitudes for the 18-mode ROM. It is clearly seen that the scaling introduced in Eq. (4.3) is effective: even though the response is rapidly increasing the normalized work of the aerodynamic forces stays essentially constant.

Having established the appropriateness of $\overline{W}_{aero}$, its value during the LCO responses obtained with the linear stiffness/ nonlinear damping ROMs (9- and 18-modes) was next determined and is shown in Figure 4.36 as a function of the dissipation modulus for the altitudes considered. Note that the normalized aerodynamic work per cycle computed for the LCOs with the 18-mode ROM has a rather linearly decreasing trend (with the exception of the 4000 ft altitude case) consistent with the linearly increasing trend of the frequencies, see Figure 4.20. Moreover, for the 9-mode ROM, the work is nearly constant as the dissipation modulus changes, again consistently with the LCO frequency.

These observations confirm the suggestion of Section 4.3 that the increased participation in the response of the torsion mode in the 18-mode LCO results affects not only the frequency of the LCO, see Figure 4.20, but also the aerodynamics. More specifically, it reduces the energy input in the system by the aerodynamics thereby providing a reduction of the response, and LCO amplitude. This property is likely, at least partially, responsible for the lower amplitude of LCO observed with this model vs. the 9-mode one which does not lead to change in the participation of the torsion mode.

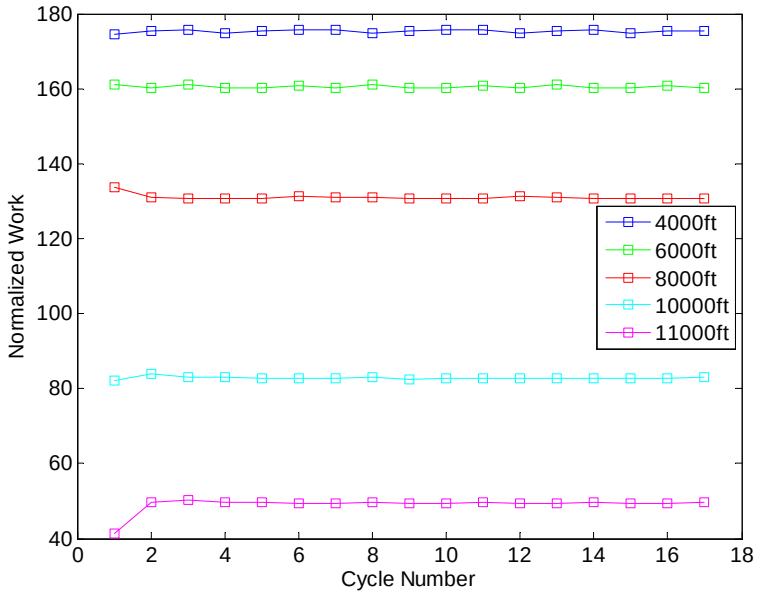

Figure 4.35. Normalized Aerodynamic Work per Cycle $\overline{W}_{aero}$ as a Function of the Cycle Number, Response at Flutter at Different Altitudes 18-Mode ROM.

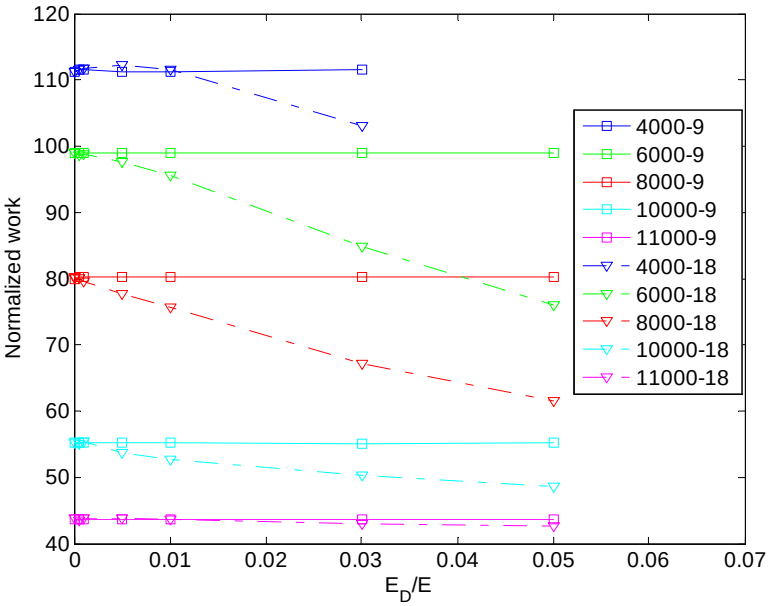

Figure 4.36. Normalized Aerodynamic Work per Cycle $\overline{W}_{aero}$ as a Function of the Dissipation Modulus E_D for Various Altitudes, ν_D = 0, 18-Mode and 9-Mode ROMs (Curves "Altitude-18" and "Altitude-9", Respectively).

5. SUMMARY

The focus of the present investigation was on the formulation, development, and a preliminary assessment of a nonlinear structural damping model that is consistent with a linear viscoelastic material undergoing large deformations. The model was developed in a reduced order modeling format assuming a Kelvin-Voigt constitutive relation expressed in the undeformed configuration and led to governing equations for the generalized coordinates in the form of van der Pol – Duffing equations. These equations which generalize similar reduced order models obtained for elastic structures are parametric, i.e., involve a series of coefficients which are functions of the material properties, geometry of the structure, and basis functions used to represent the response. An existing identification strategy of the stiffness parameters in such reduced order models was next modified to permit the determination of the linear and nonlinear damping coefficients.

The application that is of particular interest here for the assessment of the nonlinear damping model is the post-flutter response of wings and most notably the occurrence of some limit cycle oscillations (LCO) which are not fully understood but thought to potentially arise from structural damping nonlinearity. The Goland wing was selected as the structure of interest because of the public availability of its structural finite element model and of a commercially developed time-domain model of its aerodynamics.

The development of the reduced order model started with the selection of the basis functions, a set of linear modes but also dual modes to capture accurately the in-plane, mostly spanwise, displacements which occur in nonlinear geometric conditions but not linear ones. Next was the identification of the stiffness coefficients and then a set of

validations carried out in comparison with nonlinear full finite element static solutions which demonstrate the applicability of the ROM for the proposed effort.

The identification of the nonlinear damping coefficients was performed next and permitted the evaluation of the nonlinear structural damping model as the “bounding” mechanism to induce LCO from flutter. This analysis was carried out with three different models characterized by linear stiffness and nonlinear damping, nonlinear stiffness and linear damping, and finally nonlinear stiffness and nonlinear damping. It was found that the nonlinear damping can indeed, even with linear stiffness properties, lead to LCO of amplitudes that can range from below 1% of span to significant fractions of this length. The consideration of linear damping and nonlinear stiffness also led to LCO but at larger levels. These results suggested the possibility to “calibrate” the nonlinear damping model from experimentally observed LCO amplitudes. Finally, the frequency of the LCO responses was also analyzed and was observed to correlate to the relative amplitudes of the responses in the first bending and torsion modes present in the limit cycle oscillations.

REFERENCES

Bonet, J., and Wood, R.D.. 1997. *Nonlinear continuum mechanics for finite element analysis*. Cambridge: Cambridge University Press.

Brignac W.J.. 1989. Limit cycle oscillation F-16 experience. *Aerospace Flutter and Dynamics Council*. 10-11 May.

Capiez-Lernout, E., Soize, C., and Mignolet, M.P.. 2012. Computational stochastic statics of an uncertain curved structure with geometrical nonlinearity in three-dimensional elasticity. *Computational Mechanics*. Vol. 49 (No. 1): 87-97.

Capiez-Lernout, E., Soize, C., and Mignolet, M.P.. 2014. Post-buckling nonlinear static and dynamical analyses of uncertain cylindrical shells and experimental validation. *Computer Methods in Applied Mechanics and Engineering*. Vol. 271: 210-230.

Chen, P.C., Lee, H.W., and Liu, D.D.. 1993. Unsteady subsonic aerodynamics for bodies and wings with external stores including wake effects. *Journal of Aircraft.* Vol. 30 (No. 5): 618-628.

Chen, P.C., Sarhaddi, D., and Liu, D.D.. 1998. Limit cycle oscillation studies of a fighter with external stores. *AIAA*. 98-1727: 258-266.

Choi, G.G., Agelastos, A.M., Mignolet, M.P., and Liu, D.D.. 2004. Effects of internal friction on the dynamic behavior of aeroelastic systems. *Proceedings of the 45th Structures, Structural Dynamics, and Materials Conference.* Palm Springs, California, Apr. 19-22. Paper AIAA-2004-1591.

Choi, G.G., Agelastos, A.M, Mignolet, M.P., and Liu, D.D.. 2005. On the impact of internal friction on flutter onset and limit cycle oscillations amplitude. *International Forum on Aeroelasticity and Structural Dynamics 2005*. Munich, Germany, Jun. 28-Jul. 1: Paper IF-022.

Denegri Jr., C.M.. 2000. Limit cycle oscillation flight test results of a fighter with external stores. *Journal of Aircraft.* Vol. 37 (No. 5) Sept.-Oct.: 761-769.

Eastep, F.E., Khot, N.S., Beran, P.S., Zweber, J.V., and Snyder, R.D.. 2002. Investigation of shock-induced LCO of a wing/store configuration using the transonic small disturbance method. *Proceedings of the 23rd Congress of the International Council on the Aeronautical Sciences (ICAS)*. Toronto, Canada, Sept. 8-13: 445.1-445.10.

Farhat, C., Geuzaine, P., and Brown, G.. 2003. Application of a three-field nonlinear fluid-structure formulation to the prediction of the aeroelastic parameters of an F-16 fighter. *Computers and Fluids.* Vol. 32 (No. 1): 3-29

Fung, Y.C., and Tong, P.. 2001. *Classical and computational solid mechanics.* River Edge, New Jersey: World Scientific.

Goland, M., and Luke, Y.. 1948. The flutter of a uniform wing with tip weights. *Journal of Applied Mechanics*. Vol. 15 (No. 3): 13-20.

Kim, K., Khanna, V., Wang, X.Q., and Mignolet, M.P.. 2009. Nonlinear reduced order modeling of flat cantilevered structures. *Proceedings of the 50th Structures, Structural Dynamics, and Materials Conference*. Palm Springs, California, May 4-7. AIAA Paper AIAA-2009-2492.

Kim, K., Radu, A.G., Wang, X.Q., and Mignolet, M.P.. 2013. Nonlinear reduced order modeling of isotropic and functionally graded plates. *International Journal of Non-Linear Mechanics*, Vol. 49: 100-110.

Kingsbury, D.W., Agelastos, A.M., Dietz, G., Mignolet, M.P., Liu, D.D., and Schewe, G.. 2005. Limit cycle oscillations of aeroelastic systems with internal friction in the transonic domain - experimental results. *Proceedings of the 46th Structures, Structural Dynamics, and Materials Conference*. Austin, Texas. Apr. 18-21, 2005. AIAA Paper AIAA-2005-1914.

Mignolet, M.P., Przekop, A., Rizzi, S.A, and Spottswood, S.M.. 2013. A review of indirect/non-intrusive reduced order modeling of nonlinear geometric structures. *Journal of Sound and Vibration*. Vol. 332 (No. 10): 2437-2460.

Mignolet, M.P., and Soize, C.. 2008. Stochastic reduced order models for uncertain geometrically nonlinear dynamical systems. *Computer Methods in Applied Mechanics and Engineering*. Vol. 197: 3951-3963.

Muravyov, A.A., and Rizzi, S.A.. 2003. Determination of nonlinear stiffness with application to random vibration of geometrically nonlinear structures. *Computers and Structures*. Vol. 81: 1513-1523.

Norton, W.J.. 1990. Limit cycle oscillation and flight flutter testing. *Proceeds of the 21st Annual Symposium*. Society of Flight Test Engineers, Lancaster, CA. 3.4-3.4-12.

Parananta, B.B., Kok, J.C., Spekreijse, S.P. Hounjet, M.H.L., and Meijer, J.J.. 2003. Simulation of limit cycle oscillation of fighter aircraft at moderate angle of attack. *NLR-TP*. 2003-526: 1-38.

Pasiliao, C. L.. 2012. Characterization of aero-structural interaction flow-field physics. *Aerospace Flutter and Dynamics Council Fall Meeting*. Shalimar, FL. 25-26 October.

Perez, R., Wang, X.Q., and Mignolet, M.P.. 2011. Nonlinear reduced order models for thermoelastodynamic response of isotropic and FGM panels. *AIAA Journal*, Vol. 49 (No. 3): 630-641.

Perez, R.A., Wang, X.Q., and Mignolet, M.P.. 2014. Non-intrusive structural dynamic reduced order modeling for large deformations: Enhancements for complex structures. *Journal of Computational and Nonlinear Dynamics*. Vol. 9 (No. 3): 031008-1 - 031008-12.

Sharma, V.K., and Denegri, C.M.. 2013. Time domain aeroelastic solution using exact aerodynamic influence coefficients and nonlinear damping. *Proceedings of the International Forum on Aeroelasticity and Structural Dynamics Society, London, 2013*. IFASD-2013-29D: 1-11.

Wang, X.Q., and Mignolet, M.P.. 2015. Personal communication.

Wang, X.Q., Perez, R., Mignolet, M.P., Capillon, R., and Soize, C.. 2013. Nonlinear reduced order modeling of complex wing models. *Proceedings of the 54th Structures, Structural Dynamics and Materials Conference*. Boston, Massachusetts. Apr. 8-11. AIAA Paper AIAA-2013-1520.

Zona Technology, Inc.. 2011. "*ZAERO Theoretical Manual*". http://www.zonatech.com /Documentation/ZAERO_THEORETICAL_MANUAL_8.5.pdf.